U.S. DEPARTMENT OF ENERGY

Prepared for the U.S. Department of Energy
under Contract DE-AC05-76RL01830

PNNL-20278
EMSP-RPT-007

Mathematical Model of Cold Cap—Preliminary One-Dimensional Model Development

R Pokorny
PR Hrma

March 2011

Pacific Northwest
NATIONAL LABORATORY

Proudly Operated by Battelle Since 1965

DISCLAIMER

This report was prepared as an account of work sponsored by an agency of the United States Government. Neither the United States Government nor any agency thereof, nor Battelle Memorial Institute, nor any of their employees, makes **any warranty, express or implied, or assumes any legal liability or responsibility for the accuracy, completeness, or usefulness of any information, apparatus, product, or process disclosed, or represents that its use would not infringe privately owned rights**. Reference herein to any specific commercial product, process, or service by trade name, trademark, manufacturer, or otherwise does not necessarily constitute or imply its endorsement, recommendation, or favoring by the United States Government or any agency thereof, or Battelle Memorial Institute. The views and opinions of authors expressed herein do not necessarily state or reflect those of the United States Government or any agency thereof.

PACIFIC NORTHWEST NATIONAL LABORATORY
operated by
BATTELLE
for the
UNITED STATES DEPARTMENT OF ENERGY
under Contract DE-AC05-76RL01830

Printed in the United States of America

Available to DOE and DOE contractors from the
Office of Scientific and Technical Information,
P.O. Box 62, Oak Ridge, TN 37831-0062;
ph: (865) 576-8401
fax: (865) 576 5728
email: reports@adonis.osti.gov

Available to the public from the National Technical Information Service,
U.S. Department of Commerce, 5285 Port Royal Rd., Springfield, VA 22161
ph: (800) 553-6847
fax: (703) 605-6900
email: orders@nits.fedworld.gov
online ordering: http://www.ntis.gov/ordering.htm

PNNL-20278
EMSP-RPT-007

Mathematical Model of Cold Cap—Preliminary One-Dimensional Model Development

R Pokorny
PR Hrma

March 2011

Prepared for
the U.S. Department of Energy
under Contract DE-AC05-76RL01830

Pacific Northwest National Laboratory
Richland, Washington 99352

Summary

The ultimate goal of studies of cold-cap behavior in glass melters, whether by batch-melting studies, laboratory-scale or large-scale melter experiments, or mathematical modeling, is to increase the rate of glass processing in an energy-efficient manner. Mathematical models are not merely an intermediate step between laboratory-scale and large-scale studies, but are also an important tool for assessing the responses of melters to vast combinations of process parameters. In the simplest melting situation considered in this study, a cold cap of uniform thickness rests on a pool of molten glass from which it receives a steady uniform heat flux. Thus, as the feed-to-glass conversion proceeds, the temperature, velocity, and extent of feed reactions are functions of the position along the vertical coordinate, and these variables do not change with time. Using this model, we present the sensitivity analyses on the effects of key parameters on the cold-cap behavior. The second part of the report presents an insight to the phenomenon of batch foaming and shows that for a reliable prediction of the melting rate as a function of feed properties and melter conditions; future work has to focus on the behavior of the foam layer at the bottom of the cold cap and the heat transfer through it.

Acknowledgments

Pacific Northwest National Laboratory is operated for the U.S. Department of Energy by Battelle under Contract DE-AC05-76RL01830. The authors are grateful to the U.S. Department of Energy's Hanford Tank Waste Treatment and Immobilization Plant Project Office Engineering Division for financial support and Albert Kruger for his assistance and guidance. The authors would like to acknowledge the help of Dong-Sang Kim for his suggestions and discussions about the waste glass melting process, Jaehun Chun for his kind review, and the help of other colleagues who kindly provided all experimental data.

Acronyms and Abbreviations

1D, 2D, 3D	one, two, and three dimensional
ANL	Argonne National Laboratory
DSC	differential scanning calorimetry
EGA	evolved gas analysis
HLW	high-level waste
SRNL	Savannah River National Laboratory
TGA	thermal gravimetric analysis
WTP	Hanford Tank Waste Treatment and Immobilization Plant

List of Symbols

A	area	m^2
c	heat capacity	kJ kg^{-1} K^{-1}
g	gravitational constant	m s^{-2}
h	heat transfer coefficient	W $m^{-2}K^{-1}$
h	thickness	m
H	heat source	W m^{-2}
ΔH	heat flux	W m^{-2}
j	mass flux	kg m^{-2} s^{-1}
L	characteristic length	m
N	melting rate	kg m^{-2} s^{-1}
Nu	Nusselt number	1
q	heat flux	W m^{-2}
Q	heat flux	W m^{-2}
r	radial coordinate	m
Ra	Rayleigh number	1
s	heat flux	W m^{-2}
t	time	s
T	temperature	K
v	velocity	m s^{-1}
V	volume	m^3
x	global coordinate	m
β	thermal expansion coefficient	m^{-1}
δ	space step	m
ε	absolute tolerance	K
ε	emissivity	1
λ	thermal conductivity	W $K^{-1}m^{-1}$
μ	dynamic viscosity	Pa s
ν	kinematic viscosity	m^2 s^{-1}
ξ	degree of conversion	1
ρ	density	kg m^{-3}
τ	time step	s
Φ	void fraction	1

Contents

Figures

Tables

1.0 Introduction

The cost and schedule of high-level waste (HLW) treatment is highly dependent on the loading of HLW in glass and on the rate of HLW glass production. Increasing the rate of glass processing in the Hanford Tank Waste Treatment and Immobilization Plant (WTP) at Hanford will allow shortening the life cycle of waste cleanup. Melting rate studies are being performed to develop a fundamental understanding of the glass conversion reactions, in particular those that strongly influence the rate of melting, and models to predict the impacts of composition and other key parameters on the melting rate, which will be used to identify the methods and strategy to increase the throughput of HLW feeds.

Many factors impact the performance of glass processing during vitrification process in an all-electrical melter. One of the most important, and also one of the least understood, is the process of batch melting. It is thus of great importance to better understand this process.

In the simplest case, one can consider a steady vertical melting of a typical waste glass batch, floating on the surface of glass melt (the so-called "cold cap"). In such a batch layer, many processes are taking place:

- water evaporation (slurry feed contains as high as 60% of water)
- gas evolution
- the melting of salts
- the formation of borate melt
- reactions of borate melt with molten salts and with amorphous Fe_2O_3 and Al_2O_3
- the formation of intermediate crystalline phases
- the formation of a continuous glass-forming melt
- the growth and collapse of primary foam
- the dissolution of residual solids.

To this list, we also need to add the formation of secondary foam originating from molten glass, but accumulating on the bottom of the cold cap.

Very little attention was paid to the conversion process within the cold cap in the past (Hrma et al. 2009, Hrma 1982, Schill 1982a, 1982b) because the heat transfer to the cold cap rather than the batch-to-glass conversion itself has been considered as rate-controlling. However, according to Hrma (1990), the melting only becomes conversion-controlled if the heat flux to the batch blanket is high enough.

In accordance with the Project Quality Assurance Plan (PQAP) for the Environmental Management (EM)-31 Support Project, this work was designated as Quality Level 3 (QL3). This designation is based on the fact that the work is exploratory (experimental) in nature and will not be used directly for the design or operation of vitrification facilities. As such, the work was performed in accordance with best laboratory practices, Nuclear Quality Assurance (NQA)-1, Subpart 4.2, and it was based on work flows

and subject areas of the Pacific Northwest National Laboratory (PNNL) “How do I…?” (HDI) standards based management system.

This study presents the latest developments in the mathematical modeling of the cold cap behavior during batch melting. As the first step, we developed a preliminary one-dimensional (1D) model. To represent more fully the situation that exists in an all-electrical melter, our final goal is to develop a 3D model that will represent the melt-rate affecting processes more realistically. The preliminary version of the 1D model of this report describes the progress of feed melting reactions in a vertical direction with the constitutive equations and key parameters based on data obtained for a specific feed denoted as A0 (Hrma et al. 2009). The interfaces with glass melt and plenum space are defined by simplified boundary conditions. The results of feed melting crucible studies, in addition to literature data, will be used as input data for the model. The method for computing the melting rate has not yet been finalized; therefore, the objective of this report is to establish a background for further modeling. Although the study is focused on a batch for HLW vitrification, the authors hope that the outcome will also be relevant for commercial glass melting.

2.0 Theory on the Cold Cap Modeling

2.1 Assumptions

It is important to point out that our model is based on the previously developed models described by Hrma (1982) and Schill (1982a, 1982b).

Glass batch, or melter feed, is a heterogeneous mixture of different solids and liquids. The composition of A0 feed designed to vitrify high-alumina HLW is presented in Table 2.1.

Table 2.1. A0 Batch Compositions (in g) to Make 1 kg of Glass

Compound	g/kg
$Al(OH)_3$	367.49
$B(OH)_3$	269.83
$Bi(OH)_3$	12.80
$CaCO_3$	0.00
$Ca(NO_3)_2{\cdot}4H_2O$	0.00
CaO	60.79
$Fe(H_2PO_2)_3$	12.42
$Fe(OH)_3$	73.82
K_2CO_3	0.00
KNO_3	3.04
Li_2CO_3	88.30
$LiNO_3$	0.00
$Mg(OH)_2$	1.69
NaF	14.78
$NaNO_2$	3.37
$NaNO_3$	4.93
NaOH	97.14
Na_2CO_3	0.00
$Na_2C_2O_4$	1.76
Na_2CrO_4	11.13
Na_2SO_4	3.55
$NiCO_3$	6.36
$Ni(NO_3)_2{\cdot}6H_2O$	0.00
$PbCO_3$	0.00
$Pb(NO_3)_2$	6.08
SiO_2	305.05
$Zn(NO_3)_2{\cdot}4H_2O$	2.67
ZnO	0.00
$Zr(OH)_4{\cdot}xH_2O$	5.11
Totals	1352.10

It is clear that during the melting of such a batch, many overlapping reactions occur: producing gases, such as CO_x, or NO_x, liquids, and intermediate solids, such as spinel. In an electrical melter, individual phases move, possibly with different velocities. For simplicity, we consider a two-phase model in which the feed is a mixture of the condensed phase comprising liquids and solids, and the gas phase.

Figure 2.1 illustrates an electrical melter during melting. The slurry is fed to the melter from the top, creating a cold cap resting on a pool of molten glass. Molten glass then leaves the melter through the glass discharge port. The 1D model views the cold cap as a blanket of a uniform thickness resting on a pool of molten glass from which it receives a steady uniform heat flux (Figure 2.2).

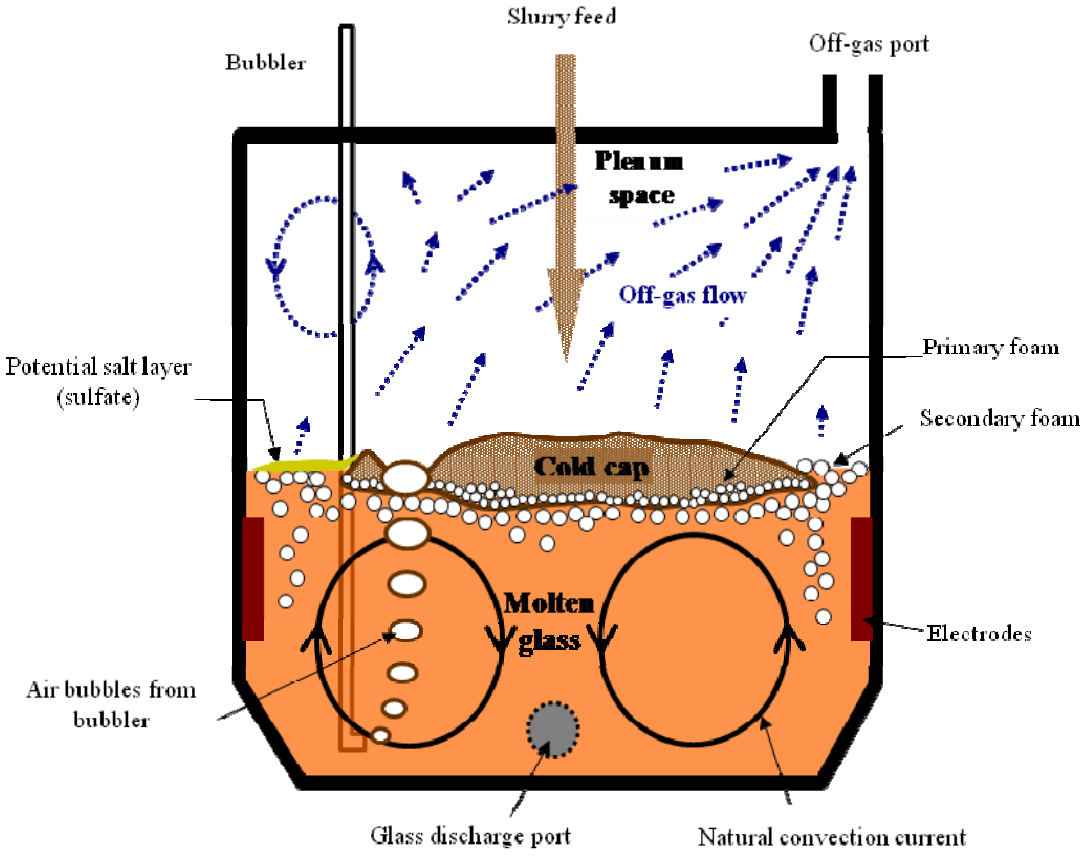

Figure 2.1. Schematic Illustration of Electrical Melter

Under optimal steady-state conditions, the slurry feed is charged from above onto the surface of the cold cap to maintain its thickness. Each feed particle travels vertically down through the cold cap, experiencing increasing temperature in response to which its properties are changing: density, dissolution rates of solids, reaction kinetics, etc. Thus, as the feed-to-glass conversion proceeds, the temperature, velocity, and extent of feed reactions are functions of the position along the vertical coordinate, and these variables do not change with time.

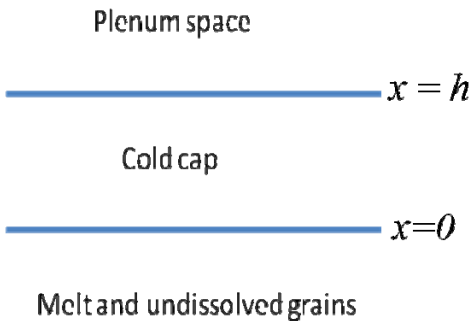

Figure 2.2. Cold Cap During Steady-State Conditions

2.2 Mass Balance

Neglecting the diffusion, the mass balances of both condensed phase and gas phase are

$$\frac{d\rho_c}{dt} + \frac{d(\rho_c v_c)}{dx} = r_c \tag{2.1}$$

$$\frac{d\rho_g}{dt} + \frac{d(\rho_g v_g)}{dx} = r_g \tag{2.2}$$

where ρ = density
v = velocity
r = mass change rate
c and g = condensed phase and the gas phase, respectively (subscripts).

By the mass conservation law, the total mass balance is

$$r_c + r_g = 0 \tag{2.3}$$

The mass fluxes, j_i, are defined as

$$j_c = -\rho_c v_c \tag{2.4}$$

$$j_g = \rho_g v_g \tag{2.5}$$

Because the structure of cold cap material is porous, the values of bulk density, ρ_b, and bulk velocity, v_b, can be used with advantage:

$$j_c = -\rho_b v_b \tag{2.6}$$

Because the condensed phase moves in a negative direction, the minus sign is used in Equations 2.4 and 2.6 to obtain a positive flux.

The integral gas production and the total gas production are

$$N_g(x) = \int_0^x r_g \, dx \tag{2.7}$$

$$N_{gT} = \int_0^h r_g \, dx \tag{2.8}$$

where x is the vertical coordinate with the origin at the cold-cap bottom (see Figure 2.2), and h is the total thickness of the cold cap. $N_g(x)$ represents the gas production at a position x, and N_{gT} represents the gas flux leaving the cold cap from the top.

The degree of conversion with respect to the gas production is defined as

$$\xi_g(x) = 1 - N_g(x) / N_{gT} \tag{2.9}$$

With this definition, its value changes from 0 to 1.

According to the mass conservation law, the difference between the mass flux of the condensed phase to and from the cold cap (the mass loss) is:

$$\Delta j_c = j_{ch} - j_{c0} = N_{gT} \tag{2.10}$$

where j_{ch} is the mass flux of the condensed phase entering the cold cap on the top, and j_{c0} is the mass flux of the condensed phase leaving the cold cap from the bottom.

Accordingly, the mass flux of the condensed phase at any position is related to the degree of conversion with respect to gas as

$$j_c(x) = j_{ch} - \Delta j_c \xi_g(x) \tag{2.11}$$

The mass flux of the gas phase can be thus also expressed using the degree of conversion and the mass loss of the condensed phase:

$$j_g(x) = \Delta j_c \left(1 - \xi_g(x)\right) \tag{2.12}$$

satisfying the condition $j_g(h) = \Delta j_c$.

2.3 Energy Balance

Many chemical reactions and physical-chemical processes occur while the batch blanket is melting. Almost all such processes absorb and evolve heat; thus, the heating involves more than the total heat needed to raise the temperature of the batch from its feeding temperature to the temperature of glass melt. Furthermore, many other processes with an impact on the temperature distribution are present during melting. For example, the water evaporation belongs between the processes with the highest impact.

To calculate the temperature distribution within the cold cap, the following energy balance is used:

$$\rho_b c_c \frac{dT_c}{dt} = -\rho_b v_b c_c \frac{dT_c}{dx} - \frac{dq_c}{dx} + H + s \tag{2.13}$$

$$\rho_g c_g \frac{dT_g}{dt} = -\rho_g v_g c_g \frac{dT_g}{dx} - \frac{dq_g}{dx} - s \tag{2.14}$$

or in steady state form, Equations 2.13 and 2.14 have the form

$$\rho_b v_b c_c \frac{dT_c}{dx} = -\frac{dq_c}{dx} + H + s \tag{2.15}$$

$$\rho_g v_g c_g \frac{dT_g}{dx} = -\frac{dq_g}{dx} - s \tag{2.16}$$

where T = temperature
c_c and c_g = temperature dependent heat capacities of individual phases
q_c and q_g = conductive heat fluxes
H = a heat source (in the case of exothermic reactions) or heat sink (in the case of endothermic reactions)
s = heat transfer between gas phase and condensed phase throughout the cold cap.

The conductive heat fluxes can be expressed by the Fourier's law:

$$q_c = -\lambda_c \frac{dT_c}{dx} \tag{2.17}$$

$$q_g = -\lambda_g \frac{dT_g}{dx} \tag{2.18}$$

where λ_c and λ_g represent the effective values of heat conductivity of the condensed and gas phase, respectively, involving both conductive and radiative modes of heat transfer.

The values of heat conductivity naturally vary with the change in temperature and composition during the melting. The change in temperature is also accompanied with the change in structure (such as

porosity). The same problem also applies to other parameters: e.g., heat capacity, reaction heat, and density. Equation 2.13 can be thus expressed by the equation:

$$\rho_b(T,\vec{\varepsilon})c_c(T,\vec{\varepsilon})\frac{dT_c}{dt} = -\rho_b(T,\vec{\varepsilon})c_c(T,\vec{\varepsilon})v_b\frac{dT_c}{dx} - \frac{dq_c(T,\vec{\varepsilon})}{dx} + H(T,\vec{\varepsilon}) + s \tag{2.19}$$

where $\vec{\varepsilon}$ denotes the composition vector at each time.

The boundary conditions may be given in the term of fluxes, temperatures, or both:

$$q_c(0) = Q_B \tag{2.20}$$

$$q_c(h) = Q_U \tag{2.21}$$

$$T(0) = T_B \tag{2.22}$$

$$T(h) = T_U \tag{2.23}$$

where T_B and T_U represent the temperatures on the bottom and the top of the cold cap, respectively, and Q_B and Q_U represent the heat fluxes to the bottom and from the top of the cold cap, respectively.

For the solution of heat and mass balance equations, we need to express the properties of the cold cap batch as a function of temperature and composition during melting.

3.0 Estimation of Material Properties

The state of a batch at any moment during melting depends on its original state and on its melting history. This section presents experimental data used for our model calculations.

The rate of gas phase production, which is equal to the mass loss of the condensed phase, was measured in the laboratory with thermal gravimetric analysis (TGA) (Pierce et al. submitted). The TGA graph, showing the mass loss of the A0 sample during heating at different heating rates, can be seen in Figure 3.1. Figure 3.2 shows the corresponding mass loss rate where the differences between different heating rates are more distinct.

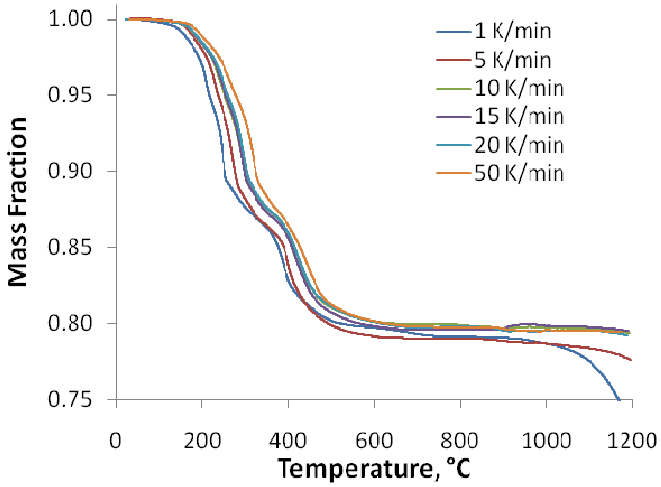

Figure 3.1. TGA Curves Showing the Mass Loss of A0 Sample at Different Heating Rates

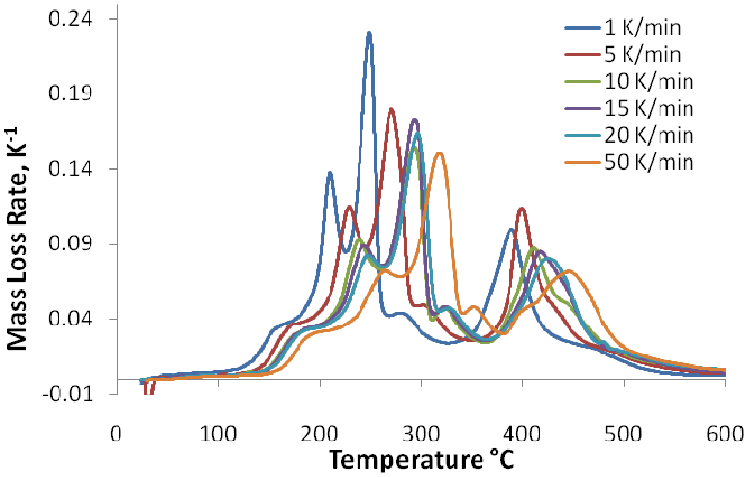

Figure 3.2. Mass Loss Rate of A0 Sample Using Different Heating Rates

Both figures indicate that the heating rate affects the melting of a batch. Unfortunately, the process of melting is rather complex, and the reaction kinetic data are not yet available in a form suitable for mathematical modeling. Thus, we are still limited to using experimental data to calculate the degree of conversion instead of precise kinetics.

The degree of conversion with respect to the gas phase ($\xi_g(T)$) is:

$$\xi_g(T) = \frac{m(T) - m_F}{m_M - m_F} \tag{3.1}$$

where $m(T)$ is the mass of the sample at temperature T, m_F is the mass of the sample at the beginning of melting, and m_M is the mass of the sample at the end of the melting when the mass of the sample is no longer changing (approximately 800°C). According to this definition, $\xi_g(T)$ varies from 0 to 1, as can be seen in Figure 3.3. The heating rate of 15 K/min was used in the model.

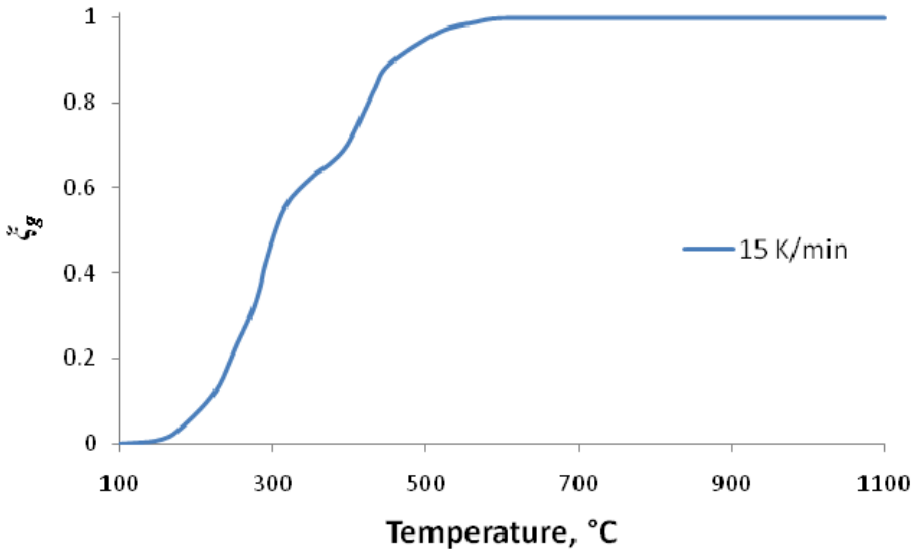

Figure 3.3. The Degree of Conversion with Respect to Gas Phase (heating rate 15 K/min)

The heat capacity of any sample is routinely measured by differential scanning calorimetry (DSC). The so called "effective" heat capacity of the A0 sample can be seen in Figure 3.4.

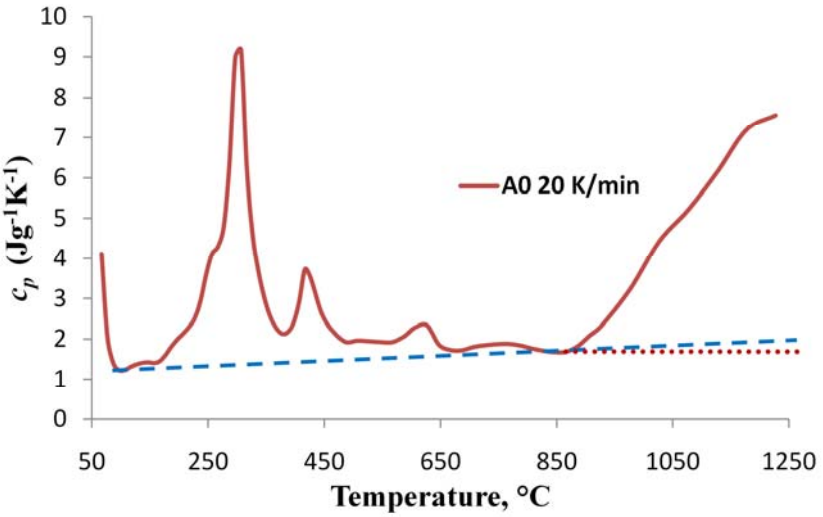

Figure 3.4. The Effective Heat Capacity of A0 Sample for Heating Rate 20 K/min. The dashed blue line indicates the possible true heat capacity of the A0 sample. The dotted red line represents the value used for $T \geq 850$°C approximated by the value at 850°C.

There are two main problems connected with calculating the true heat capacity of A0 feed. The first problem is the peaks caused by chemical reactions (releasing of bonded water and its evaporation, etc.). The reactions are mostly endothermic; they consume additional heat, thus causing an increase in heat capacity. Although we are not able to separate the reaction heat, we can use the value of effective heat capacity for the modeling of the cold cap, as will be shown later. The second problem is that the reaction peaks are shifting in response to the heating rate. At lower heating rates, the reactions have a longer time to proceed at lower temperature; thus, the position of the heat capacity peaks is changed. Although this phenomenon can be investigated more closely in the future, we are using the representative data from a fixed heating rate of 20 K/min for now.

For the modeling of the cold cap, the experimental data were taken in the interval between 100 and 850°C. The data for $T > 850$°C were approximated by the value at 850°C (represented in Figure 3.4 by the red dotted line) because of the suspected data obtained for $T > 850$°C (see Figure 3.3). All batch reactions are complete by 850°C, and the reason for such an abrupt increase is not understood. This abrupt increase at $T > 850$°C was also present during the experiment with sapphire as a reference sample; thus, it was attributed to inaccurate calibration of the DSC equipment. The blue dashed line in Figure 3.4 represents the estimation of the plausible true heat capacity value without the effect of reaction heat.

For the solution of balance equations, the heat capacity of the gas phase also needs to be known. Because the heat capacity of the gas phase has a very small effect on the batch melting, it was simply approximated by the temperature-dependent heat capacity of carbon dioxide (one of the main gas components) (Schill 1982b):

$$c_g(T) = 1003 + 0.21T - \frac{1.93 \cdot 10^7}{T^2} \quad (c_g \text{ in J/g·K and } T \text{ in K}, T \geq 373 \text{ K}) \tag{3.2}$$

Expansion measurements were conducted to understand how the density of a batch changes during melting. The result for A0 pellet expansion with a different alumina source (aluminum oxide, aluminum

hydroxide, boehmite) is displayed in Figure 3.5 (the profile area was normalized to the calculated profile area of a hemisphere that the bubble-free glass would occupy). As previously described by Henager et al. (2011), the relationship between the volume of the sample pellet and the normalized area A is proportional, although not absolutely straightforward. Even if the change in area is not so dramatic, the volume of the sample can change as much as three times. Also, the mass of the pellet decreases during heating (as shown in Figure 3.5). Figure 3.5 thus only roughly indicates the changes in the pellet density.

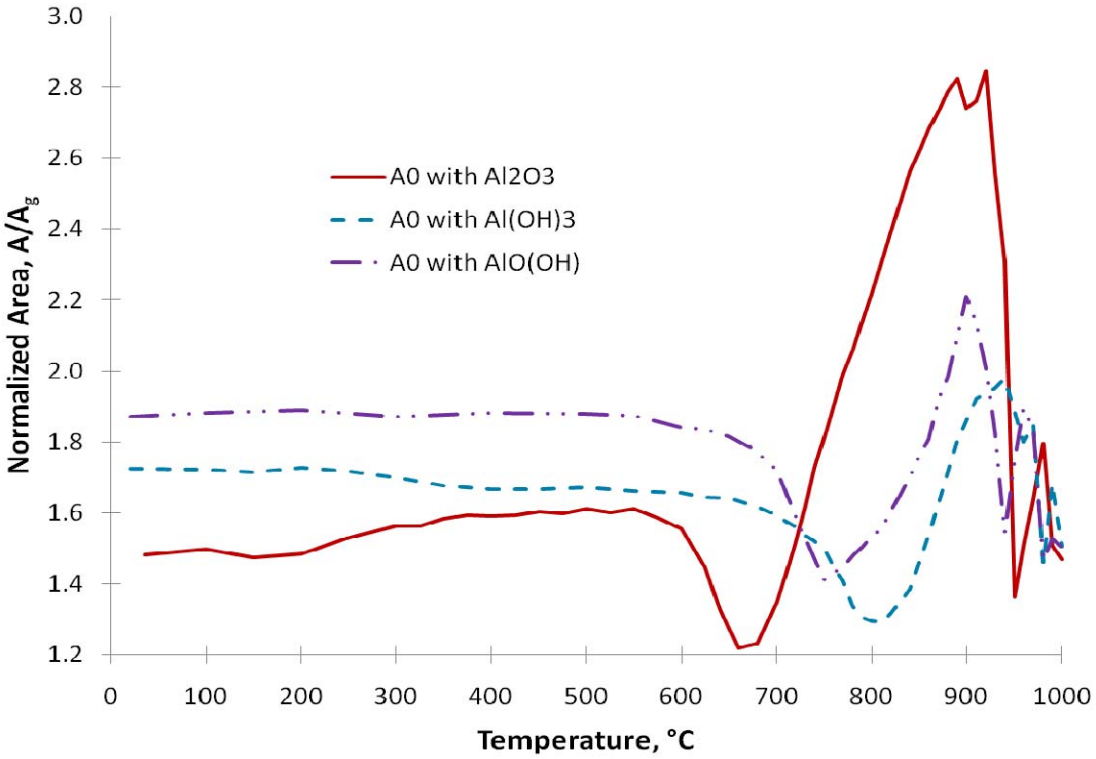

Figure 3.5. Normalized Pellet Profile Area Versus Temperature of A0 Batches with Different Alumina Source Heated at 5°C/min.

As can be seen from Figure 3.5, the normalized profile area (and thus also volume) of the batch is almost constant in the interval between 100 and 700°C (for A0 with aluminum hydroxide). Then the open porosity changes into closed porosity at about 800°C, where the minimum volume is reached. In the temperature region above 800°C, the volume is rapidly increasing because of the creation of foam. However, the expansion experiments conducted with pellets do not truly represent what happens during the melting in the batch blanket. Thus, the following data were used for the preliminary 1D modeling. Neglecting the minimum reached at 800°C, an arbitrary, but representative, value of the bulk density, ρ_b = 1300 kg/m^3, was chosen in the interval between 100 and 800°C. For the foamy area between 800 and 1100°C, where the density of the condensed phase changes rapidly to the molten glass density, the bulk density was taken to be linearly decreasing to the value ρ_b(1100°C) = 500 kg/m^3.

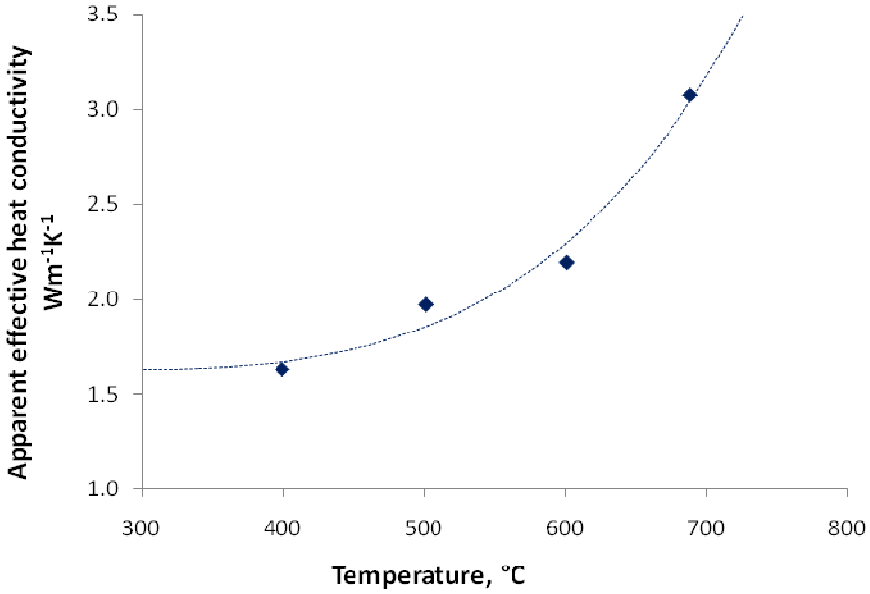

Figure 3.6. Apparent Effective Heat Conductivity Versus Temperature for Al-Na Batch

The heat conductivity of the batch was also recently measured (Hrma et al. 2010). The batch was heated in a crucible where thermocouples were positioned to measure the temperature gradient in the batch and on the crucible wall. The resulting values of the calculated "apparent" effective heat conductivity can be seen in Figure 3.6.

These values were calculated for the Al-Na batch of a composition different than, yet similar to, the A0 batch. The effective heat conductivity involves both conduction and radiation heat transfer. The true effective heat conductivity can be different from the calculated "apparent" effective one shown in Figure 3.7 because endothermic processes occurring during the batch melting affect the measured temperature gradient. Thus, the true effective heat conductivity will probably have slightly larger values. The true effective heat conductivity can be calculated with the use of calorimetric data from DSC measurements. A more detailed description can be found in Appendix A.

Figure 3.7 shows apparent effective heat conductivities of glass batches compiled from the literature.

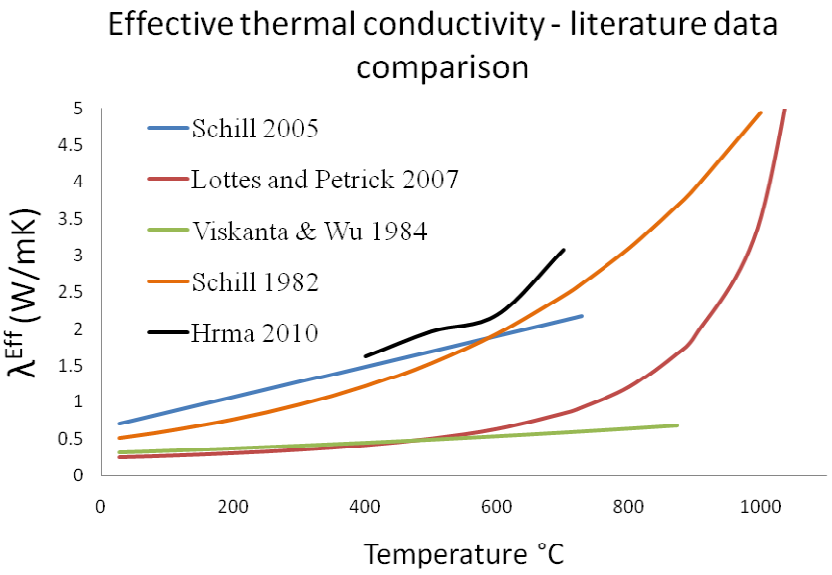

Figure 3.7. Batch Effective Heat Conductivity Versus Temperature

Note that data taken from the Argonne National Laboratory (ANL) Report 07/28 (Lottes and Petrick 2007), Viskanta and Wu (1984), and Schill (1982b) pertain to commercial batches. For our modeling, we selected data from Schill (2005):

$$\lambda^{\text{Eff}} = 0.06571 + 0.002114T \quad (\lambda \text{ in W/m·K and } T \text{ in K, } 373 \text{ K} < T < 1000 \text{ K}) \tag{3.3}$$

This relationship was previously used in Schill (2005) to model the behavior of noble metals during HLW vitrification.

In a real situation, this linear relationship is not applicable to high temperatures where the heat conductivity increases significantly as in other curves in Figure 3.7 (Schill 1982b, Lottes and Petrick 2007, Hrma et al. 2010), and thus, it cannot be used for temperatures larger than 1000 K. Similar to density, the effective heat conductivity at 1100°C (1373 K) should match that of molten glass. Thus, according to Schill (2005), Equation 3.3 is understood to be valid up to 727°C, and then the effective conductivity between 727 and 1100°C linearly increases to the value of molten glass. The value of heat conductivity at 1100°C was taken from Schill (2005), where $\lambda^{\text{Eff}}(1100°\text{C}) = 4.56$ W/m·K. The final relationship is illustrated in Figure 3.8.

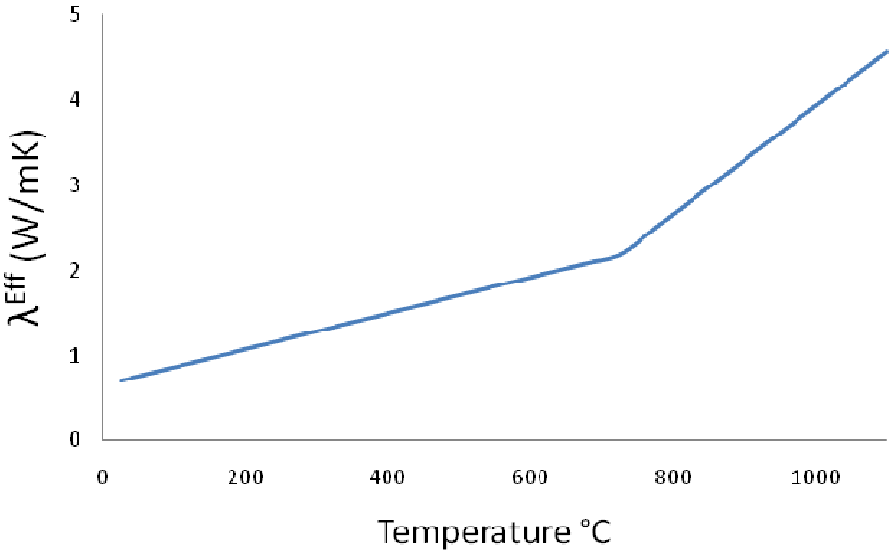

Figure 3.8. Effective Heat Conductivity Used for the Model Calculations

Also, we will use the measured experimental data as soon as they become available (see Appendix A).

4.0 Schemes for Numerical Calculations

The finite difference method was used to solve the energy balance. This method was chosen because of its simplicity and comprehensibility.

If we sum Equations 2.13 and 2.14, neglect the heat accumulation term in gas $\rho_g c_g << \rho_c c_c$, and assume the heat equilibrium between the gas and the condensed phase ($T_g = T_c$), the energy balance can be written in the form:

$$\rho_b c_c \frac{dT_c}{dt} = \left(j_c c_c - j_g c_g\right)\frac{dT_c}{dx} - \frac{dq_c}{dx} - \frac{dq_g}{dx} + H \tag{4.1}$$

Then, using explicit finite differences, we can write Equation 4.1 as a set of equations

$$\rho_{bi}^k c_{ci}^k \frac{T_i^{k+1} - T_i^k}{\tau} = \left(j_{ci}^k c_{ci}^k - j_{gi}^k c_{gi}^k\right)\frac{T_{i+1}^k - T_{i-1}^k}{2\delta} + \lambda_{i+}^k \frac{T_{i+1}^k - T_i^k}{\delta^2} - \lambda_{i-}^k \frac{T_i^k - T_{i-1}^k}{\delta^2} + H_i^k \qquad \text{i=2,..,N-1} \tag{4.2}$$

where δ represents the space step (nodal points are represented by the subscript i), and τ represents the time step (represented by the superscript k), respectively. Here, λ_{i+}^k and λ_{i-}^k are the mean values of heat conductivity between adjacent nodal points:

$$\lambda_{i+}^k = \frac{\lambda_i^k + \lambda_{i+1}^k}{2} \tag{4.3}$$

$$\lambda_{i-}^k = \frac{\lambda_i^k + \lambda_{i-1}^k}{2} \tag{4.4}$$

which represent effective values of heat conductivity of the cold cap.

For reasonably fast convergence and sufficient accuracy, the space step was usually defined to be δ = 1 mm and the time step τ = 0.1 s (the typical value of h is 100 mm; the typical value of time to reach the steady state is $50 \cdot 10^3$ s). A further decrease in the space and time step is not useful because it leads to slower convergence, and the accuracy is already at an acceptable level for our calculations. Because the heat conductivity of gas is very low, the term dq_g/dx can be neglected in Equation 2.16, and the heat transfer term between the condensed and gas phase can be expressed as:

$$s = -\rho_g v_g c_g \frac{dT}{dx} = -j_g c_g \frac{dT}{dx} \tag{4.5}$$

which represents the heat transfer between the condensed and gas phases in Equation 4.1.

However, the set of Equations in 4.2 is not complete and needs to be supplied by some type of boundary conditions, such as the Dirichlet, Neumann, or combined. Dirichlet conditions directly represent the values of boundary temperatures, for example,

$$T_1^k = 1000°\mathrm{C}$$
$$T_N^k = 100°\mathrm{C} \tag{4.6}$$

for every time step *k*. On the other hand, the Neumann boundary conditions do not define the temperature, but the heat flux. Together with the Dirichlet conditions, they can form the combined boundary conditions, in the form:

$$q_1 = \lambda_1^k \frac{T_2^k - T_1^k}{\delta} + \frac{\delta \rho_{b1}^k c_{c1}^k}{\tau}\left(T_1^{k+1} - T_1^k\right)$$
$$T_N^k = 100°\mathrm{C} \tag{4.7}$$

where q_1 is the heat flux from the melt to the cold cap:

$$q_1 = \lambda_c \left(\frac{dT}{dx}\right)_{x=0} \tag{4.8}$$

The set of finite difference equations (Equation 4.2) was iteratively solved together with chosen boundary conditions (Equation 4.6 or 4.7). The simulation was stopped when the temperature field was no longer changing in time, satisfying the condition

$$\left|\left(T_i^{k+1} - T_i^k\right)\right| \le \varepsilon \qquad \text{i=1,..,N} \tag{4.9}$$

where ε is absolute tolerance (usually $\varepsilon = 10^{-5}$ K).

The resulting temperature field was then considered as a stationary solution of Equation 2.19.

For numerical simulations, experimental data were used together with constitutive equations that were taken from the literature and modified for our problem. The mass flow of the condensed and gas phases was calculated from TGA data. Because the results from DSC experiments provide us with the effective value of heat capacity, we also needed to modify the energy balance accordingly:

$$\rho_{bi}^k c_{ci}^k \frac{T_i^{k+1} - T_i^k}{\tau} = \left(j_{ci}^k c_{ci}^{k,EFF} - j_{gi}^k c_{gi}^k\right)\frac{T_{i+1}^k - T_{i-1}^k}{2\delta} + \lambda_{i+}^k \frac{T_{i+1}^k - T_i^k}{\delta^2} - \lambda_{i-}^k \frac{T_i^k - T_{i-1}^k}{\delta^2} \tag{4.10}$$

where $c_{ci}^{k,EFF}$ represents the effective value of heat capacity, including the reaction heat:

$$j_{bi}^k c_{ci}^{k,EFF} \frac{T_{i+1}^k - T_{i-1}^k}{2\delta} = \left(j_{ci}^k c_{ci}^k\right)\frac{T_{i+1}^k - T_{i-1}^k}{2\delta} + H_i^k \tag{4.11}$$

All algorithms were coded in Matlab 7.

5.0 Results

Figure 5.1 illustrates the simplified 1D representation of the cold cap.

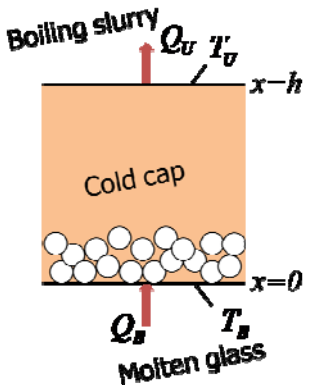

Figure 5.1. 1D Representation of Cold Cap

Possible boundary conditions considered in this case comprise the heat flux to the cold cap (Q_B), the bottom temperature (T_B), the heat flux from the cold cap (Q_U), and the upper temperature (T_U). The heat flux leaving the dry cold cap batch (Q_U) is in a real situation entering the boiling slurry above the cold cap and is consumed to preheat the slurry feed to the temperature of the boiling slurry (100°C) and to evaporate the water. As will be discussed later, the heat necessary to preheat the slurry to 100°C and to evaporate the water before the dry feed enters the cold cap is not negligible. However, in the first three parametrical studies, we assume that the heat necessary to transfer to the boiling slurry is supplied from the hot plenum space (the temperature of the plenum space is usually between 350 and 500°C), and thus, the value of the heat flux leaving the cold cap Q_U is not affected by the existence of the boiling slurry layer. The fourth parametrical study incorporates an additional situation; the heat necessary to transfer from the cold cap to the boiling slurry is known.

Bubbles on the bottom of the cold cap represent foam, which can be formed in two different ways. Primary foam is formed by the expansion of the batch by evolving the batch gases trapped in the glass-forming melt. Secondary foam is then produced in molten glass as an accumulation of fining bubbles. It is highly plausible that the foam layer has a low value of heat conductivity; thus, it hinders the heat transfer to the cold cap and leads to a lower melting rate. For the purpose of modeling, because the heat conductivity of the foam layer is not identified yet, it was estimated that the heat conductivity of the foam layer within the cold cap is equal to half of the heat conductivity of the bubble-free cold cap.

In the following sections, the feed mass flux was taken as an independent variable (parameter), although this is not a standard case in a real situation, where the mass flux is a dependent variable resulting from the melter conditions and feed properties. However, using the mass flux as a parameter is appropriate for the analyses intended in this report.

5.1 The Effect of the Mass Flux Change on the Cold Cap Thickness at a Constant Heat Flux

The results are compiled in Table 5.1 and illustrated in Figure 5.2. The temperature on the bottom of the cold cap was set to T_B = 1100°C (estimated temperature of molten glass under the foam layer), and the temperature on the upper boundary was set to T_U = 100°C (the temperature of boiling slurry pool—see Figure 5.1). The boundary temperature for the foam layer was set to 800°C where the normalized area dropped the first time, as in the feed with $Al(OH)_3$ (Figure 3.5). The mass flux j_s was increased by 1 and 2%, respectively, while the heat flux to the bottom of the cold cap was kept constant. The constant heat

flux to the cold cap (Q_B = 36.5 kW) was chosen on an arbitrary basis, but it represents a typical situation in which the constant electrode power maintains a constant melt temperature. The basic value of the mass flux was taken to be j_{ch} = 0.0177 kg/s/m^2, corresponding to the representative value of 1530 kg day/m^2.

Table 5.1. Effect of the Change in the Feed Mass Flux on the Cold Cap Thickness—Constant Heat Flux Q_B = 36.5 kW/m^2

j_{ch} [kg/s/m^2]	0.0177	0.0179	0.0181
j_c [%]	100%	101%	102%
h [cm]	10.3	10.7	11.1
Q_U [kW/m^2]	2.59	2.28	1.98

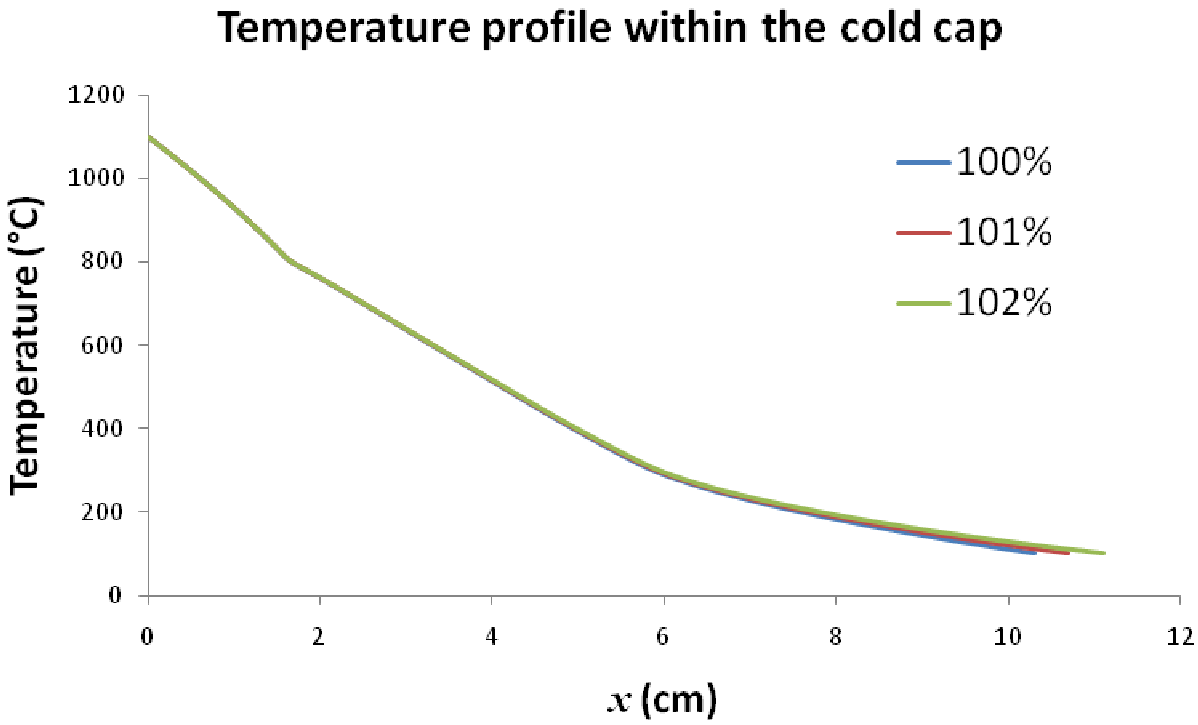

Figure 5.2. Effect of Mass Flux on Cold Cap Thickness at Constant Heat Flux

Three intervals with similar temperature gradients can be seen in Figure 5.2. The interval from 1100°C to 800°C pertains to the foam layer. The temperature gradient changes at 250 to 350°C as a result of endothermic melting reactions—see Figure 3.4.

A slight increase in the mass flux caused a remarkable increase in the cold cap thickness. According to Table 5.1, the increase in the feed mass flux by 2% (from 0.0177 to 0.0181 kg/m^2/s) resulted in an increase in the cold cap thickness of 8% (from 10.3 cm to 11.1 cm). This may explain the "frozen cold cap" that is created when insufficient heat is transferred to the cold cap. The batch feeding needs to be then stopped, leading to a loss of melter efficiency.

Q_U represents the heat flux from the top of the cold cap that can be used to heat the boiling slurry.

For an illustration, the velocity profile of the condensed phase is shown in Figure 5.3.

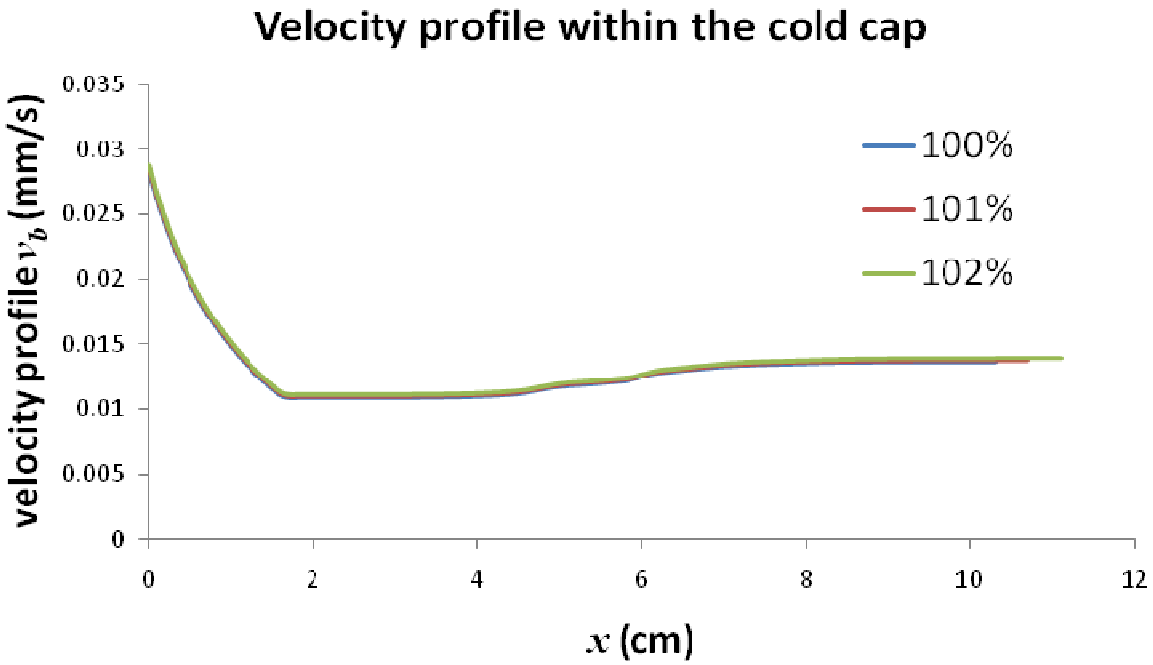

Figure 5.3. Velocity Profile Within the Cold Cap at Constant Heat Flux

Going from the top of the cold cap (x > 10 cm), the velocity of the condensed phase is constant until it starts to decrease as a result of gas evolution. The foam causes the abrupt increase in velocity at the bottom of the cold cap. Because of the higher porosity, the material needs to move faster, according to Equation 2.6.

5.2 The Effect of the Heat Flux Change on the Cold Cap Thickness at a Constant Mass Flux

This study shows the opposite effect when the mass flux is kept constant, and the heat flux from the molten glass is increased. The same boundary conditions were used (T_B = 1100°C and T_U = 100°C). The mass flux was set to be j_{ch} = 0.0177 kg/s/m^2, and the heat flux to the cold cap from the bottom was increased by 1 and 2%.

Table 5.2. Effect of the Change in the Heat Flux on the Cold Cap Thickness—Constant Mass Flux $j_{ch} = 0.0177$ kg/s/m^2

Q_B [kW/m^2]	36.53	36.93	37.30
Q_B [%]	100%	101%	102%
h [cm]	10.3	9.8	9.4
Q_U [kW/m^2]	2.59	2.99	3.36

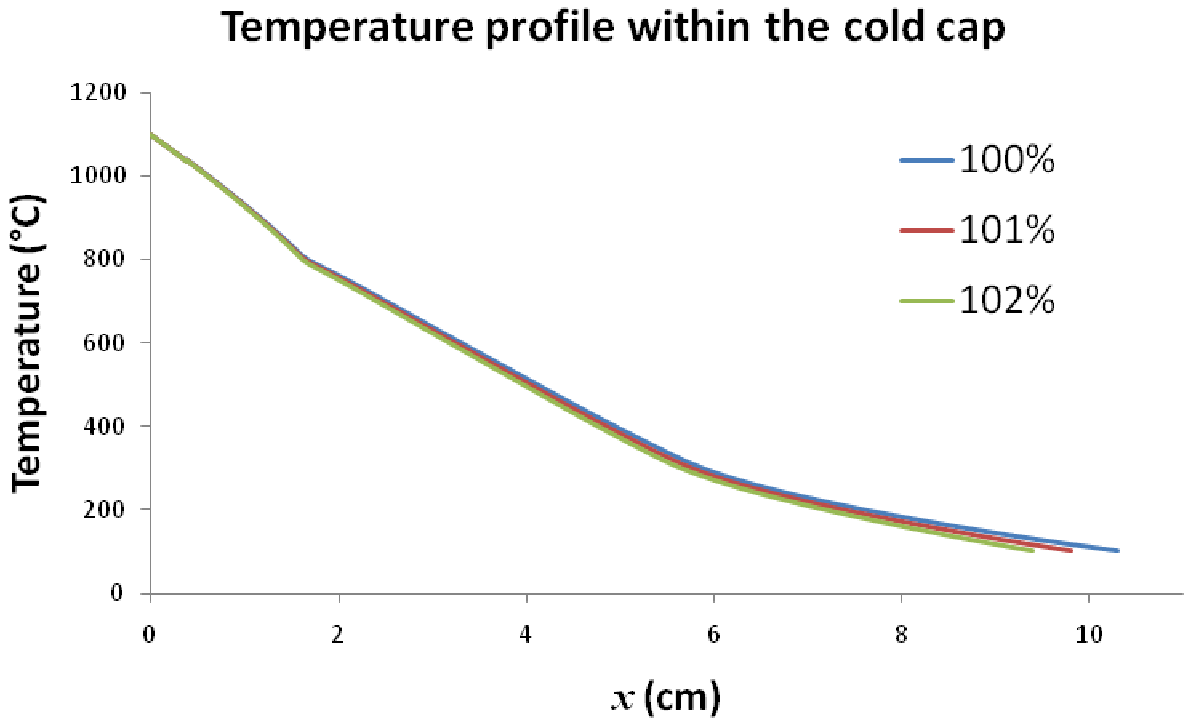

Figure 5.4. Effect of the Heat Flux on Cold Cap Thickness at Constant Mass Flux

As can be seen, the increase in the heat flux decreases the thickness of the cold cap. This result, which was expected, was a consequence of the melting heat of the material being the same in all three cases, and the thickness of the cold cap layer decreased as the heat that was transported through the cold cap increased.

5.3 The Effect of the Mass Flux Change on the Cold Cap Thickness with Modified Heat Flux

As in the previous examples, the boundary temperatures were set to $T_B = 1100$°C and $T_U = 100$°C. However, the change in the mass flux (±10%) was now accompanied with the same change in the heat flux to the cold cap (±10%). The results are compiled in Table 5.3 and illustrated in Figure 5.5.

Table 5.3. Effect of Mass Flux with Proportional Heat Flux on the Cold Cap Thickness

j_c [kg/m^2]	0.0177	0.0195	0.0160
Q_B [kW/m^2]	36.53	40.13	32.83
Q_B , j_c [%]	100%	110%	90%
h [cm]	10.3	9.5	11.2
Q_U [kW/m^2]	2.59	2.66	2.55

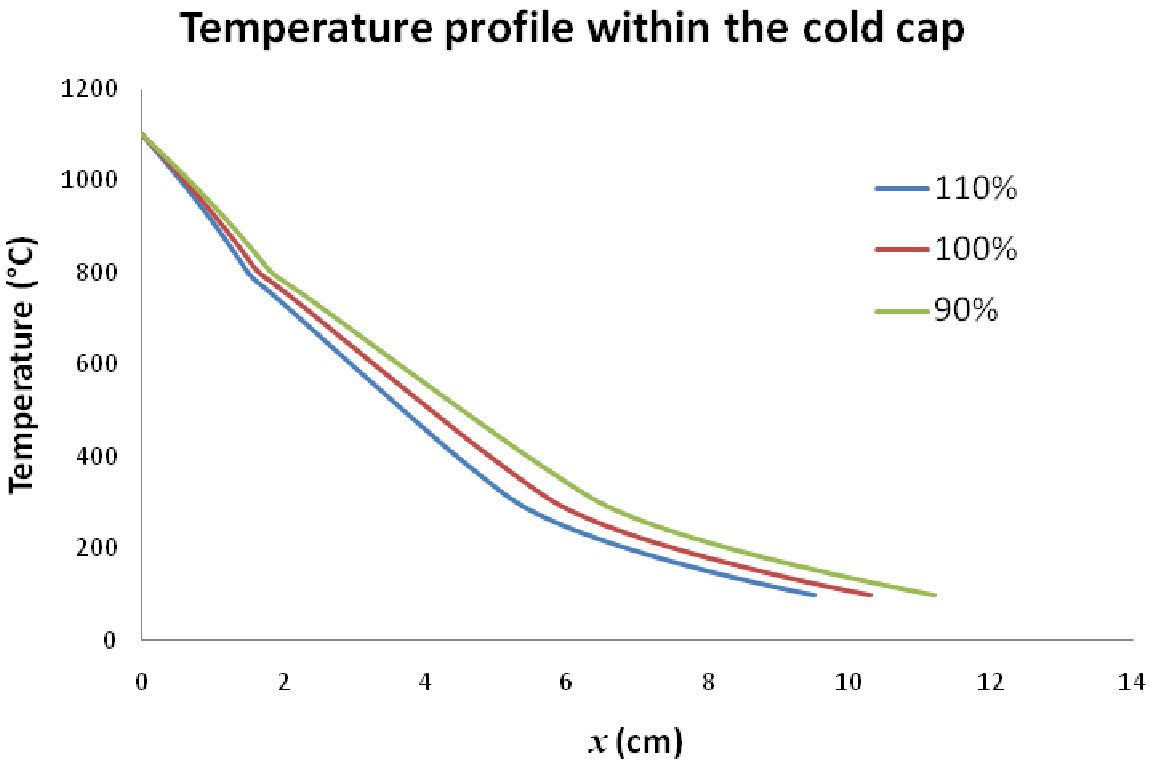

Figure 5.5. Effect of Mass Flux with Proportional Heat Flux on Cold Cap Thickness

With the heat flux increasing in proportion to the mass flux, the change in the cold cap thickness is less dramatic. It can be seen that the thickness of the cold cap is mainly controlled by the heat flux to the cold cap. Thus, if sufficient heat can be transferred to the cold cap, then the melting rate can be increased without the possibility of the "frozen cold cap" forming.

5.4 Water Evaporation

The batch is usually fed into the melter in the form of slurry containing 40 to 60% of water. The evaporation heat of water is $\Delta H_{VAP,W}$ = 2.26 MJ/kg. Furthermore, additional heat is needed to heat the vapor from 100°C to the plenum space temperature of 350 to 450°C. As an example, consider that the mass flux of the slurry feed is j_s = 0.037 kg/m^2/s with 52.2% (0.0193 kg/m^2/s) of water, so the resulting dry batch rate is again j_{ch} = 0.0177 kg/s/m^2.

The heat flux to evaporate water is

$$\Delta H_{\mathrm{VAP}} = j_{\mathrm{W}} \Delta H_{\mathrm{VAP,W}} = 0.0193 \cdot 2.26 \cdot 10^{6}\ \mathrm{W/m^2} = 43.6\ \mathrm{kW/m^2} \tag{5.1}$$

The heat flux to heat the vapor from 100°C to 350°C is

$$\Delta H_{\mathrm{STEAM}} = j_{\mathrm{STEAM}} c_{\mathrm{p,STEAM}} \left(T_2 - T_1\right) = 0.0193 \cdot 2000 \cdot \left(350 - 100\right) \mathrm{W/m^2} = 9.7\ \mathrm{kW/m^2} \tag{5.2}$$

The heat flux to melt the dry batch to molten glass (calculated from DSC data, Figure 3.4) from 100°C to 1100°C is

$$\Delta H_{\mathrm{BATCH}} = 33.8\ \mathrm{kW/m^2} \tag{5.3}$$

Thus, almost two-thirds of the total heat flux needed (53.3 kW/m^2) is consumed to heat and evaporate water.

However, the cold cap cannot cover a whole melt-surface area (typically, 90 to 95% coverage), which suggests that the heat flows from the free surface of the molten glass to the plenum space by radiation and conduction/convection. This heat flux helps to preheat the slurry, evaporate water, and heat the vapor.

Consider the following example. The heat to preheat the slurry from the feed temperature to the temperature of the boiling slurry (100°C) is

$$\begin{aligned} \Delta H_{\mathrm{PRE}} &= \left(j_{\mathrm{WATER}} c_{\mathrm{p,WATER}} + j_{\mathrm{DRYBATCH}} c_{\mathrm{p,DRYBATCH}}\right)\left(T_2 - T_1\right) = \\ &= \left(0.0193 \cdot 4185 + 0.0177 \cdot 1300\right) \cdot \left(100 - 30\right) \mathrm{W/m^2} = 7.3\ \mathrm{kW/m^2} \end{aligned} \tag{5.4}$$

The sum of the heat flux, which needs to be supplied either from the plenum space or from the molten glass (or both) is

$$\Delta H_{\mathrm{SUM\_ABOVE}} = \Delta H_{\mathrm{PRE}} + \Delta H_{\mathrm{VAP}} = 50.9\ \mathrm{kW/m^2} \tag{5.5}$$

In the real situation, the heat flux is coming both from the molten glass and from the plenum space owing to the coverage of the melt-surface area by the cold cap.

Figure 5.6 compares the temperature fields within the cold cap for three different cases. The first case corresponds to the situation where all the heat necessary to heat up the batch slurry, evaporate the water, and heat the water vapor is supplied from the cold cap, and no heat is supplied from the plenum space. Thus, the heat flux leaving the cold cap and entering the boiling slurry is Q_U = 50.9 kW/m^2, and the corresponding heat flux to the bottom of the cold cap is Q_B = 84.7 kW/m^2 ($Q_U + \Delta H_{\mathrm{BATCH}}$). The second case represents the situation where half of the heat (50% of $\Delta H_{\mathrm{SUM\_ABOVE}}$) is supplied from the plenum space (thus Q_U = 25.5 kW/m^2), and the corresponding heat flux to the molten glass is Q_B = 59.3 kW/m^2. The third case eventually represents the situation where even more heat is supplied from the plenum space (80% $\Delta H_{\mathrm{SUM\_ABOVE}}$) (thus Q_U = 10.2 kW/m^2), and the corresponding Q_B = 44.0 kW/m^2. Note that the total heat flux supplied to the slurry layer is a constant.

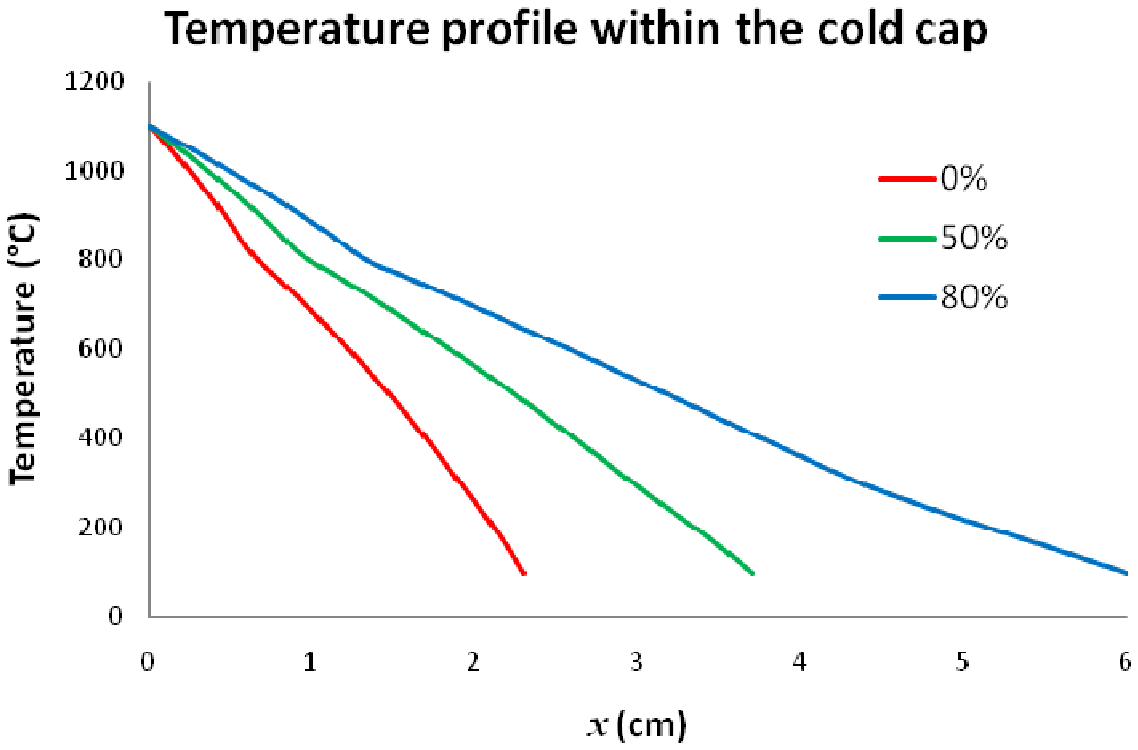

Figure 5.6. Temperature Field Within the Cold Cap for Different Portions of Heat Flux from Plenum Space

As the heat flux from the plenum space increases, a thicker cold cap is formed, resulting in a lower heating rate. As discussed in Section 6.3, a lower heating rate results in a lower foaming. When a substantial part of the heat is supplied from molten glass, large foaming occurs, which can lead to a decrease in the melting rate (Section 6.3).

6.0 Melting of Foaming Batches

The ultimate goal of our research is, not surprisingly, to enhance the melting rate to improve the waste loading capacity of the HLW melter. As was previously shown by Hrma (1990), the melting rate is influenced not only by the heat transfer to the cold cap, but also by the reaction kinetics. In one of his papers (Hrma 1990), Hrma derived following relationship for the melting rate N:

$$N = \frac{N_C^2}{2N_H}\left(\sqrt{1+\frac{4N_H^2}{N_C^2}}-1\right) \tag{6.1}$$

where

$$N_C = \sqrt{\frac{\lambda_F k\rho(T_I - T_F)}{Q}} \tag{6.2}$$

is the ultimate melting rate achievable by enhancing heat transfer without changing the conversion kinetics and

$$N_H = \frac{\lambda_M (T_M - T_I)}{\delta Q} \tag{6.3}$$

is the heat transfer-controlled melting rate

where λ_F = effective heat conductivity of the cold cap
k = conversion rate coefficient
ρ = feed density
T_F = feed temperature at the beginning of conversion reactions
T_I = temperature at the cold cap-melt interface
Q = conversion heat
λ_M = effective heat conductivity of the melt under the cold cap
T_M = melter operating temperature
δ = temperature boundary layer thickness in the melt under the cold cap.

By Equation 6.1, the melting rate will be conversion controlled ($N \to N_C$) if the conversion rate is low ($k \to 0$), or the heat transfer rate is high ($\delta \to 0$). Under these theoretical conditions, the melting rate will be determined by the physical and chemical characteristics of the conversion layer (reaction kinetics, etc.) and will be no longer affected by the conditions of the glass melt pool, except for the melting temperature.

However, according to recent melter experiments, even if the heat transfer to the cold cap is extremely high, the melting rate is not solely affected by batch-to-glass conversion.

Figure 3.1 shows that the mass loss (the conversion progress) of the A0 batch is not substantially affected by the heating rate. Even if a sufficient heat flux is supplied to the cold cap so that the A0 batch will experience a very rapid heating rate of 50 K/min, the conversion kinetics plays a negligible role. Although the gas evolving reactions start slightly later with a higher heating rate, they end at the narrow temperature interval of 600 to 650°C. During batch melting, the heating rate experienced by particles in the cold cap usually varies between 5 and 20°C/min.

The rate-controlling step is thus still the heat transfer from the molten glass to the cold cap. However, the chemical and physical characteristics of the batch are important because they strongly affect the heat transfer.

6.1 Primary and Secondary Foam

The heat transfer to the cold cap is greatly influenced by the heat transfer through the layers of primary and secondary foam at the bottom of the cold cap. As was mentioned before, the primary foam is formed by gases evolved in the lower layer of the cold cap after the borosilicate glass-forming melt becomes continuous. Primary foam collapses when enough gas is evolved and when the viscosity of the melt becomes low enough to cause the melt films separating the cells to break (approximately 900°C---see Figure 3.5). The secondary foam is formed by the presence of gas bubbles produced in the molten glass. Because of the buoyancy force, these bubbles are rising to the surface and accumulate under the cold cap.

The primary foam can be decreased, and perhaps entirely eliminated, by an appropriate formulation and preparation of the batch feed. For the extent of foaming during melting, see Figure 3.5 (batch feeds with different sources of alumina) and Figure 6.1 (batches with different sizes of silica grains).

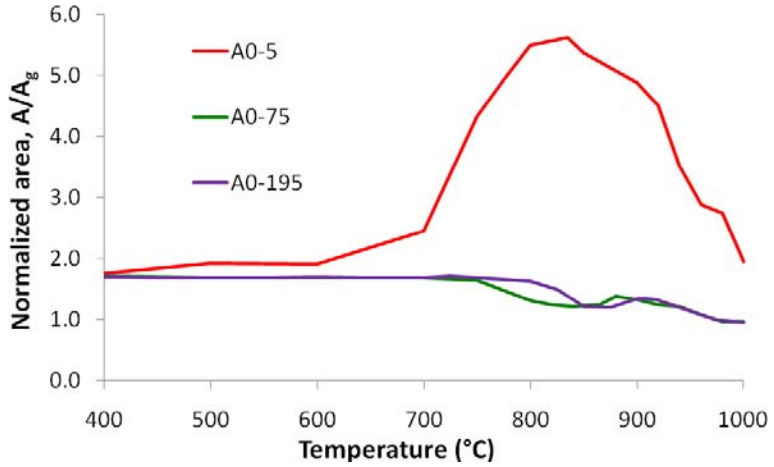

Figure 6.1. Relative Pellet Profile Area Versus Temperature of A0 Batches Heated at 5 K/min with Silica Grains of 5 μm, 75 μm, and 175 μm in Size

The extent of secondary foam can also be decreased by bubbling. Big bubbles created by the bubbler absorb smaller bubbles evolved in the melt. In addition, these large bubbles create vent holes through the cold cap through which gas escapes to the plenum space without accumulating under the cold cap. In addition, hot bubbles also act as a heat source to heat up the plenum space and eventually also to heat the slurry on the top of the cold cap.

Bubbling also enhances the convection in molten glass, significantly increasing the heat flux from the melt to the batch, resulting in a higher melting rate. The relationship between the intensity of bubbling and the specific production capacity (melting rate), showing a strong correlation, can be found in Perez et al. (2005).

The melting rate depends primarily on the heat flux transported through the foam layer on the bottom of the cold cap. A quantitative relationship has been obtained between the glass production rate and the bubbling rate (Perez et al. 2005).

6.2 Foam Layer—Structure Models

Consider a cold cap from the A0 feed with Al_2O_3. As Figure 3.5 shows, this feed exhibits a high expansion. The gas evolved below T_P = 660°C escapes through the open pores, thus slightly affecting the density of the material. At approximately 550°C, the first borosilicate melt forms, reducing the volume of the pellet. At approximately T_P = 660°C, the melt becomes connected, and the open porosity turns into closed porosity. At this point, the evolving gas becomes trapped in the high-viscosity melt. At higher temperatures, the cold cap becomes more and more porous. This continues until approximately T_S = 900°C when enough gas is evolved, and the viscosity (which is exponentially decreasing with temperature) becomes low enough to cause the melt films separating the cells to break. Primary foam escapes into large cavities of secondary foam that move to the sides of the cold cap or the vent holes.

Gases from redox reactions that are evolving in the molten glass are trapped at the bottom of the cold cap. The boundary between the secondary foam layer and the primary foam is T_S = 900°C in this case. Bubbles are not capable of penetrating above this boundary because the melt is too viscous.

The bottom temperature of secondary foam depends on the thickness of the so-called “thermal boundary layer” below the foam layer under the cold cap. However, because of strong convection in the molten glass, this thermal boundary layer is thin. Moreover, the effective thermal diffusivity of the foam layer is much lower than the thermal diffusivity of molten glass, and the temperature within the thin thermal boundary layer will be little affected. We can assume that T_B is between 1050 and 1150°C. The corresponding cold cap structure that can be used for modeling is illustrated in Figure 6.2.

This structure can be compared with cold-cap samples collected during melting of HLW glass batches. Figure 6.3 displays X-Ray images by Choi and colleagues from Savannah River National Laboratory (SRNL) (Choi et al. 2010). The batch was melted in a Pt beaker from the bottom for 22 minutes. Figure 6.4 shows a cold cap that formed during the melting of HLW glass in a laboratory-scale melter. In both examples, we can see how foam separates the melting feed in the cold cap from the molten glass.

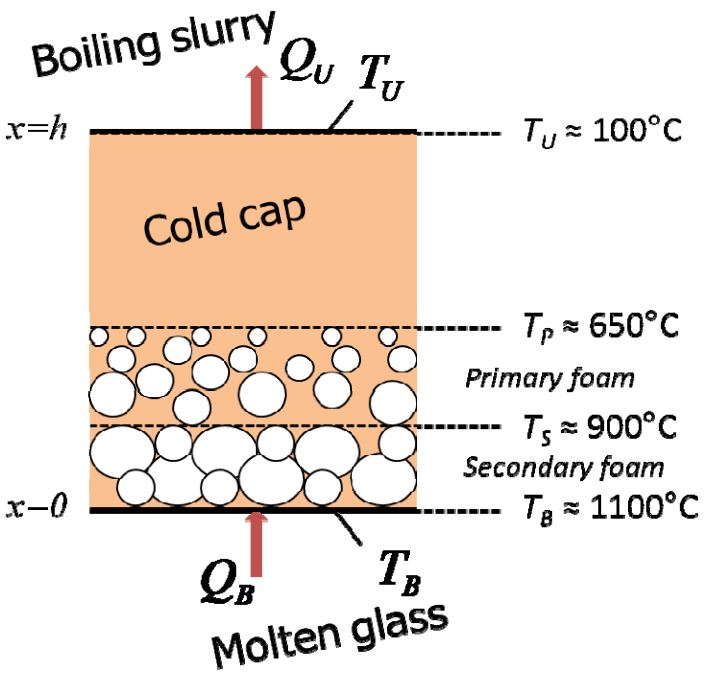

Figure 6.2. The Illustration of the Cold Cap Model Layers

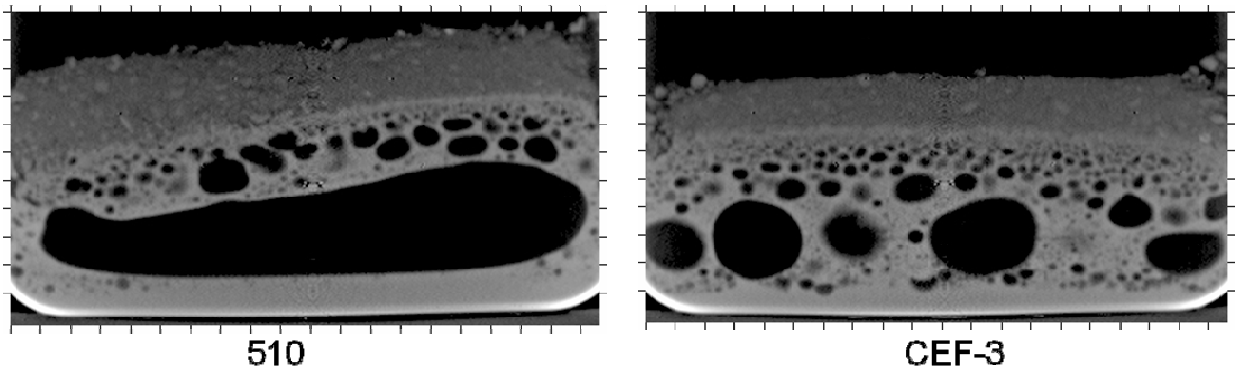

Figure 6.3. The X-Ray Image of Melted Batches (courtesy of Choi SRNL, 2010)

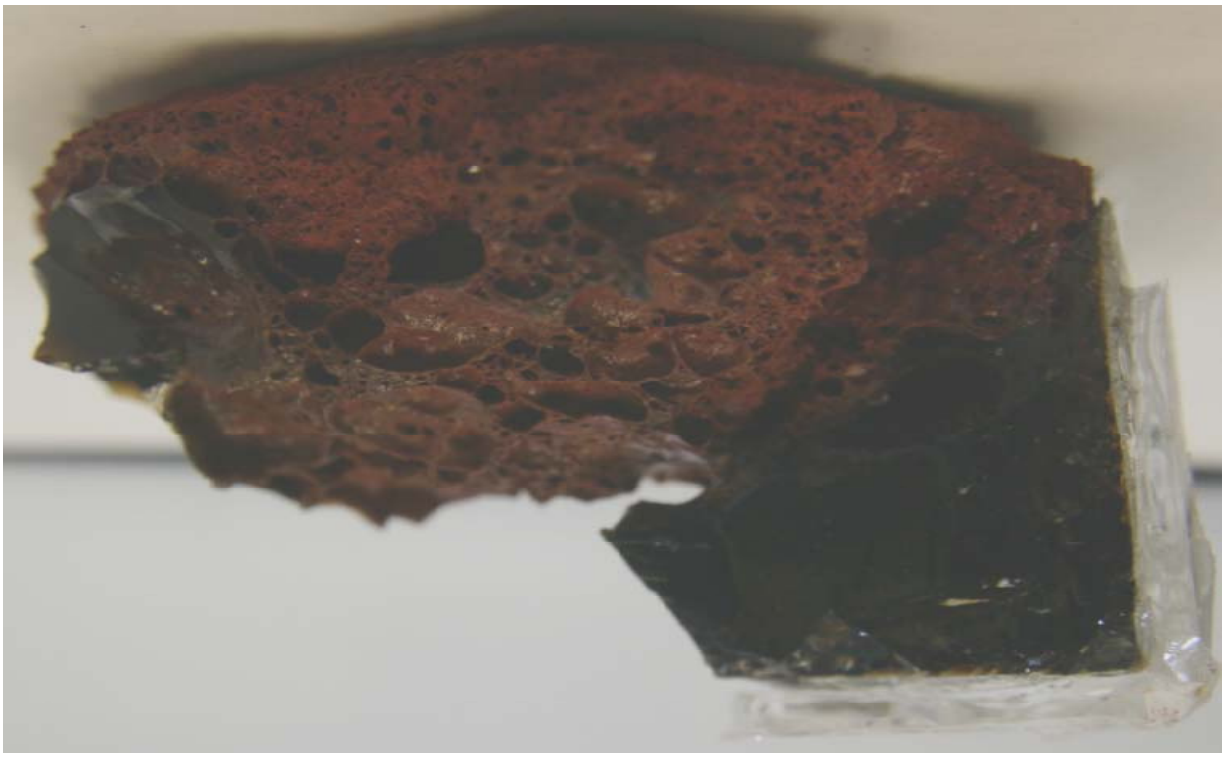

Figure 6.4. Bottom of the Cold Cap Created During Melting of HLW

However, the previous model is based on one important assumption: in the primary foam region, the viscosity is so high that the gas bubbles cannot move and are dragged down with the condensed phase. The validity of this assumption can be in the first approximation studied by the use of the so-called Stokes law:

$$v_u = \frac{2}{9}\frac{(\rho_M - \rho_G)}{\mu} g R^2 \tag{6.4}$$

where ρ_M and ρ_G are the density of the condensed melt and evolved gas, respectively, μ is the dynamic viscosity of the melt, and R is the radius of the evolved gas bubble. The resulting v_u is the velocity of the gas bubble caused by buoyancy.

Table 6.1 shows the calculated values of v_u for a different bubble radius and viscosity of the melt (ρ_M = 2300 kg/m^3, ρ_G was neglected, and g = 10 ms^{-2}).

Table 6.1. Calculated Velocity of the Bubble. Green Zone Represents the Rising Bubbles.

		bubble diameter						
		10 mm	5 mm	1000 µm	500 µm	200 µm	100 µm	50 µm
log (μ)	μ (Pa.s)	velocity (m/s)						
0	1.00E+00	1.28E-01	3.19E-02	1.28E-03	3.19E-04	5.11E-05	1.28E-05	3.19E-06
0.25	1.78E+00	7.19E-02	1.80E-02	7.19E-04	1.80E-04	2.87E-05	7.19E-06	1.80E-06
0.5	3.16E+00	4.04E-02	1.01E-02	4.04E-04	1.01E-04	1.62E-05	4.04E-06	1.01E-06
0.75	5.62E+00	2.27E-02	5.68E-03	2.27E-04	5.68E-05	9.09E-06	2.27E-06	5.68E-07
1	1.00E+01	1.28E-02	3.19E-03	1.28E-04	3.19E-05	5.11E-06	1.28E-06	3.19E-07
1.25	1.78E+01	7.19E-03	1.80E-03	7.19E-05	1.80E-05	2.87E-06	7.19E-07	1.80E-07
1.5	3.16E+01	4.04E-03	1.01E-03	4.04E-05	1.01E-05	1.62E-06	4.04E-07	1.01E-07
1.75	5.62E+01	2.27E-03	5.68E-04	2.27E-05	5.68E-06	9.09E-07	2.27E-07	5.68E-08
2	1.00E+02	1.28E-03	3.19E-04	1.28E-05	3.19E-06	5.11E-07	1.28E-07	3.19E-08
2.25	1.78E+02	7.19E-04	1.80E-04	7.19E-06	1.80E-06	2.87E-07	7.19E-08	1.80E-08
2.5	3.16E+02	4.04E-04	1.01E-04	4.04E-06	1.01E-06	1.62E-07	4.04E-08	1.01E-08
2.75	5.62E+02	2.27E-04	5.68E-05	2.27E-06	5.68E-07	9.09E-08	2.27E-08	5.68E-09
3	1.00E+03	1.28E-04	3.19E-05	1.28E-06	3.19E-07	5.11E-08	1.28E-08	3.19E-09
3.25	1.78E+03	7.19E-05	1.80E-05	7.19E-07	1.80E-07	2.87E-08	7.19E-09	1.80E-09
3.5	3.16E+03	4.04E-05	1.01E-05	4.04E-07	1.01E-07	1.62E-08	4.04E-09	1.01E-09
3.75	5.62E+03	2.27E-05	5.68E-06	2.27E-07	5.68E-08	9.09E-09	2.27E-09	5.68E-10
4	1.00E+04	1.28E-05	3.19E-06	1.28E-07	3.19E-08	5.11E-09	1.28E-09	3.19E-10

Using a melting rate of 1550 kg/m^2/day, the ρ_M = 2300 kg/m^3, the porosity in the primary foam layer 40%, the correlated melt velocity was calculated to be approximately 1.30E-5 m/s. The velocity of gas bubbles needs to overcome this melt velocity to rise up since gas bubbles and melt move in opposite directions. This means that if the viscosity of the melt is $\mu = 10^4$ Pa·s, then even very large bubbles in the range of 1 cm can be dragged down to the secondary foam layer region. However, if the viscosity of the glass-forming melt is lower (for example, $\mu = 10^2$ Pa·s), then only small bubbles (<1 mm) will be dragged down with the melt. However, because of the continuous gas evolution, these bubbles will grow until they reach a critical value of approximately 1 mm, and then they will rise up against the down-moving melt, reach the open porosity layer, and escape to plenum space. This will result in one foam layer where no inner boundary is present, as in the previous model. Following the previous example with A0 feed, a possible cold cap structure in the case of the low viscosity melt is illustrated in Figure 6.5.

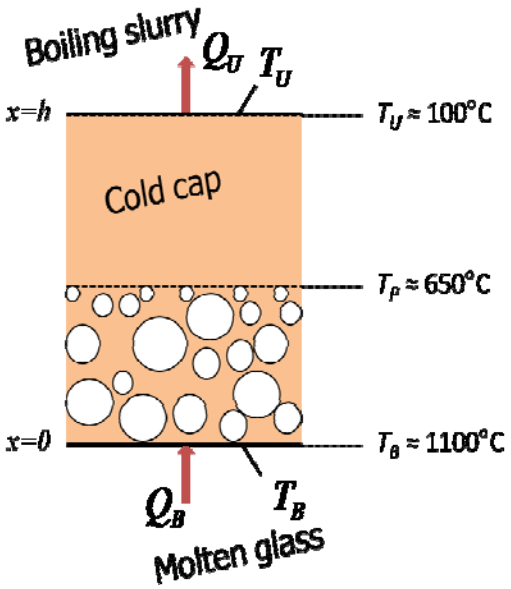

Figure 6.5. Foam Layer (low-viscosity melt)

6.3 Effect of Heating Rate on the Foaming of the Glass Batch

Consider a situation when foam is not present. Then the bottom of the cold cap is exposed to the temperature of the molten glass, the heat transfer to the cold cap is high, and the melting rate is conversion controlled. The gas evolution measured by TGA is not sufficient to define the conversion progress because it does not represent the conversion until the end of the melting process. The batch expansion data may provide an alternative. Raether and Kraus (2004) measured the effect of the heating rate on the batch expansion. In their experiments, the change in the heating rate leads to a significant change in the batch melting behavior.

Consider the impact of this relationship on the cold cap. At a low mass flow, the batch particles are exposed to a low heating rate. According to Raether and Kraus (2004), the foaming is also low, and enough heat is transferred to melt the material. Therefore, the mass flow can be increased. Consequently, the heating rate becomes higher. In turn, the batch will move faster through the cold cap. Thus, the temperature gradient will be steeper, also contributing to a higher heating rate. This phenomenon can be seen in Figure 6.6 where the cold cap thickness was kept constant (h = 5 cm), and the mass flux was increased from $j_s(50\%) = 0.0089$ kg/m^2/s to $j_s(100\%) = 0.0177$ kg/m^2/s and to $j_s(200\%) = 0.0354$ kg/m^2/s.

According to Raether and Kraus (2004), the higher heating rate will then result in higher foaming. Because less heat can be transferred to the cold cap through a thicker foam layer, the thickness of the cold cap will increase, and the rate of melting will decrease, even leading to cold–cap freezing as discussed in Section 5.1 if the mass feeding is not decreased according to the actual melting rate.

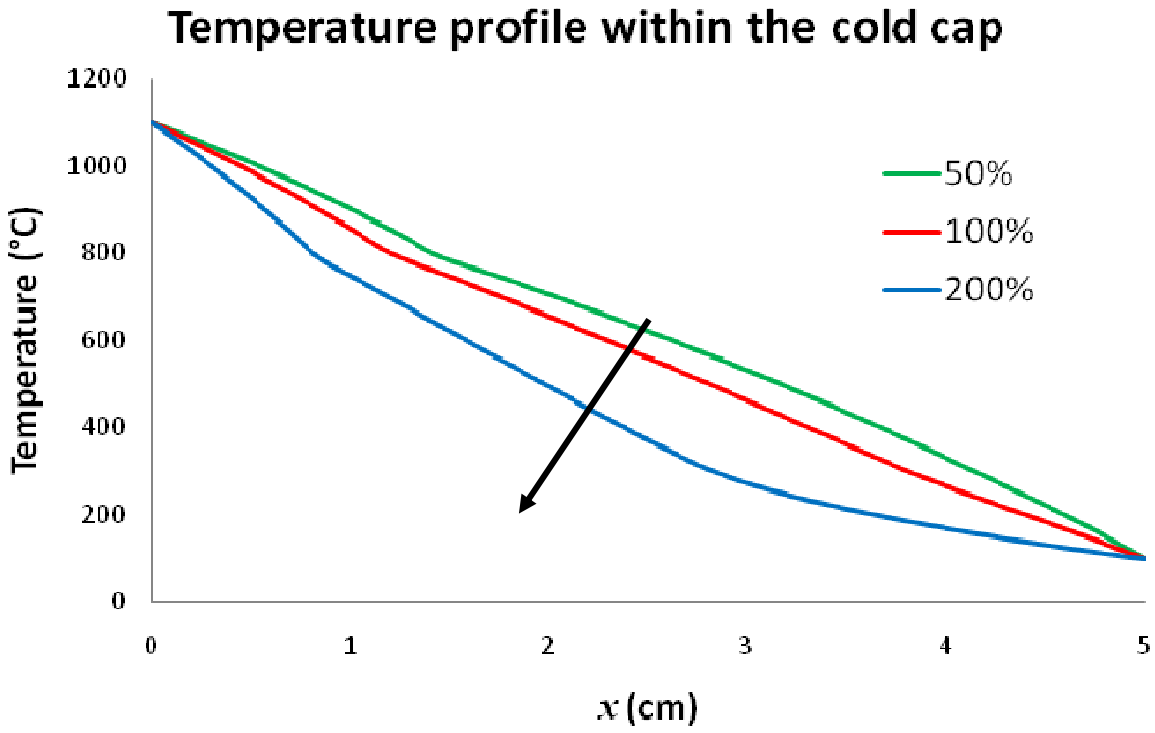

Figure 6.6. Temperature Profile Within the Cold Cap at Different Mass Fluxes, j_s. Arrow indicates increase in heat flux.

6.4 Heat Transfer in Primary and Secondary Foam

As shown previously, the heat transfer through the foam layer is the rate-controlling process for glass batch melting in an all-electric melter. This section addresses the three possible mechanisms of the heat transfer through foam, i.e., conduction, convection, and radiation.

By Fourier's law, using representative values, the conductive heat flux is

$$Q_{\text{conduction}} = \lambda_{FOAM} \frac{T_2 - T_1}{\delta_{Foam}} = 0.5 \frac{1100 - 800}{0.05} = 3000 \text{ W/m}^2 = 3 \text{ kW/m}^2 \tag{6.5}$$

The conduction heat increases as the foam layer thickness (δ_{Foam}) decreases.

The Rayleigh criterion for the onset of gas convection in a gas bubble is

$$\text{Ra} = \frac{g\beta(T_2 - T_1)L^3}{\nu\lambda} \tag{6.6}$$

where g = gravitational constant (m/s^2)
β = thermal expansion coefficient (K^{-1})
T_2 and T_1 = foam boundary temperatures (K)
ν = kinematic viscosity (m^2/s)
λ = heat conductivity of gas inside the bubble
L = characteristic length (m), which corresponds to the distance between the colder (T_1) and warmer (T_2) surface, in this case approximated by the gas bubble dimension ($L = \delta_{Foam}$).

Convection sets in when the Rayleigh number is higher than the critical values of 650 to 1700. This is the case for a large bubble (cavity) of 2 and 5 cm, and the typical values of other parameters are

$$\mathrm{Ra} = \frac{9.81 \times 0.001 \times (1100 - 800) \times 0.02^3}{138.6 \times 10^{-6} \times 3.0 \times 10^{-4}} \cong 600 < \mathrm{Ra}_{\mathrm{Critical}} \tag{6.7}$$

$$\mathrm{Ra} = \frac{9.81 \times 0.001 \times (1100 - 800) \times 0.05^3}{138.6 \times 10^{-6} \times 3.0 \times 10^{-4}} \cong 9000 > \mathrm{Ra}_{\mathrm{Critical}} \tag{6.8}$$

Hence, gas bubbles need to be sufficiently large for the convection to start. For $\mathrm{Ra} > \mathrm{Ra}_{\mathrm{Critical}}$, the convective heat flux can then be calculated:

$$\mathrm{Ra} \Rightarrow \mathrm{Nu} \Rightarrow h \Rightarrow Q_{\mathrm{convection}} \approx 2000 - 3000\ \mathrm{W/m^2} = 2 - 3\ \mathrm{kW/m^2} \tag{6.9}$$

where Nu = Nusselt number
h = convective heat transfer coefficient
$\mathrm{Nu} = 0.54\ \mathrm{Ra}^{1/4}$
$h = \mathrm{Nu} * \lambda / L$
$Q_{\mathrm{convection}} = h(T_2 - T_1)$.

This relationship for Nu is valid for the free convection between horizontal plates at $10^4 < \mathrm{Ra} < 10^7$, which is the best possible representation of our situation.

The convective heat transfer operates only for large bubbles with a high temperature gradient across them. Even if these bubbles can exist, the convective heat transfer through them is almost negligible.

The radiation between two parallel surfaces with known emissivity can be expressed as

$$\mathrm{Q}_{\mathrm{radiation}} = \frac{\sigma\left(T_2^4 - T_1^4\right)}{\frac{1}{\varepsilon_1} + \frac{1}{\varepsilon_2} - 1} = \frac{\sigma\left(1100^4 - 800^4\right)}{\frac{1}{0.70} + \frac{1}{0.88} - 1} \cong 40000\ \mathrm{W/m^2} = 40\ \mathrm{kW/m^2} \tag{6.10}$$

where σ is the Stefan-Boltzmann constant ($\sigma = 5.67 \times 10^{-8}$ Wm^{-2}K^{-4}), and $\varepsilon_1 = 0.70$ and $\varepsilon_2 = 0.88$ are the emissivities of the cold cap and molten glass, respectively (taken from Viskanta [1984]). When compared to the heat transfer by conduction (and possibly convection), the radiation heat transfer is dominating.

However, Equation 6.6 is only valid for parallel plates. In bubbles, the radiation heat can significantly differ. Because the radiation is also scattered by the foam, the radiation heat transfer decreases with the increase in foam layer thickness, thus following the same trend as the heat conduction.

As was shown in this section, the heat transfer in the foam layer is complicated, mainly because of uncertainty in the determination of thermal radiation. We also need to point out that the temperature of the melt dragged by incoming bubbles can influence the temperature of the secondary foam.

7.0 Cold Cap Behavior in Different Melters

7.1 Thickness of the Cold Cap

When comparing the melting rate in two different melters, very similar results are usually obtained for the same melter conditions (intensity of bubbling, molten glass temperature, cold cap coverage, etc.). Cold cap shapes illustrated in Figure 7.1 are possible if the thickness of the cold cap is defined by spreading of the feed material on the molten glass surface (melter A is larger than melter B):

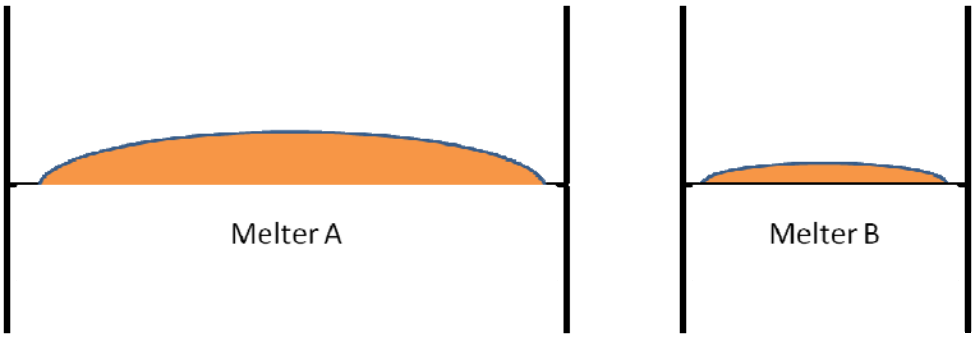

Figure 7.1. The Cold Cap Thickness Is Defined by Spreading

If this is the situation in real melters, the cold cap will have a different thickness in both melters. Because the experimental results show us that the melting rate is comparable in both smaller and larger melters and thus the velocity of the material in the cold cap is similar, then the time that a particle spends in the cold cap will be longer in the case of a larger melter with a thicker cold cap. Thus, the species in the cold cap will experience a different heating rate, and the cold cap behavior will not be the same; as we already showed, a larger heating rate will result in larger foaming, which is accompanied with a lower heat flux through the foam layer. The lower heat flux will then result in a lower melting rate. This is a contradiction of what we actually see in the melters because, as already mentioned, the melting rates are similar in melters with different sizes. The only noticeable exception is a very small laboratory melter where the effects of walls start to play a significant role (cold cap bridging, etc.).

However, we know that the melting rate in smaller melters is not lower than in larger melters. The following picture shows another case—the cold cap thickness is not defined by spreading, but is defined by the heat necessary to transport through the cold cap to the boiling slurry. It was shown previously (and according to Fourier's law) how the thickness of the cold cap depends on the heat transfer through the cold cap. This thickness is not affected by the surface area of the cold cap, but only by the heat transfer (see Figure 7.2).

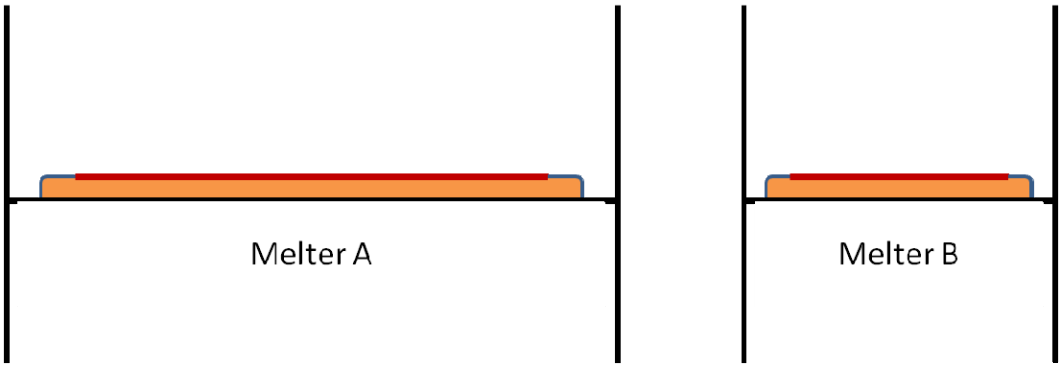

Figure 7.2. The Cold Cap Thickness Is Defined by Heat Transfer (red line on the top of the cold cap represents the boiling slurry)

In this case, the thickness of the cold cap will be same in both cases, resulting in a similar heating rate, similar foaming, and a similar melting rate. Thus, it is possible that the second case will happen during the melting process. The idea that the cold cap thickness depends on heat transfer was also supported by a personal communication with Innocent Joseph from Energy Solutions; the cold cap thickness for HLW feeds seems not much different between larger and smaller melters. Another supporting fact for the second case is based on the melting experiments—when observing the cold cap during melting, we can see the presence of the boiling slurry pool, surrounded by a small region of dried feed, which is then surrounded by the molten glass.

7.2 Bubble Layer Under the Cold Cap—Conceptual Model

The gas layer under the cold cap is formed from the gas evolving by fining reactions in the molten glass and by gas evolved during batch reactions in the closed-porosity zone. If we assume that the cold cap is too viscous for the gas bubbles to penetrate, then the gas in the layer under the cold cap will move to the sides of the cold cap or to the vent holes (created mostly by bubbling) where it can escape to the plenum space.

The estimation of the gas layer thickness under the cold cap (considered for now as a solid surface representing a barrier for the evolved gases) is not very straightforward. The shape of the layer will depend on its "minimum of energy," which consists of the potential energy due to gravitational force and the surface energy. However, it can be shown that the thickness of this layer depends on the width of the cold cap (the diameter of the cold cap when observing from above) and on the "wettability" of the cold cap surface (Iguchi and Ilegbusi 2010). Although the estimation of the wettability is very uncertain, it can be assumed that it will be almost constant for all feeds.

The important phenomenon in estimating the thickness of the gas layer is as follows. When the cold cap width reaches a certain minimal value (in the range of centimeters), the thickness of the gas layer under the cold cap will remain constant. If no vent holes are created by bubbling, the following situation will happen during melting (Figure 7.3):

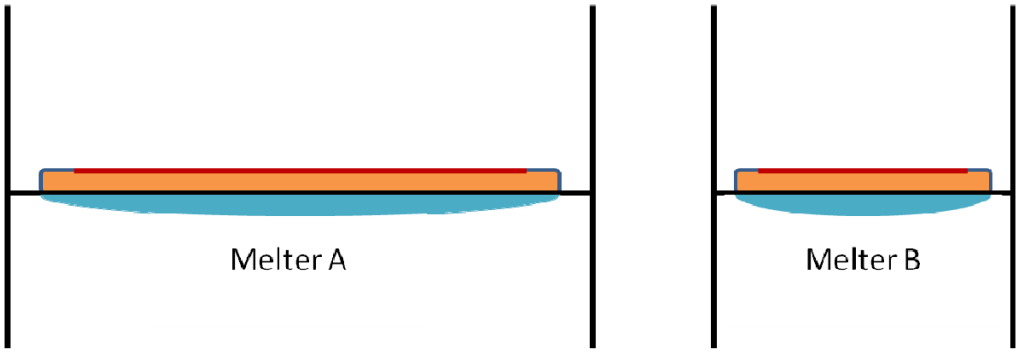

Figure 7.3. Gas Layer Under the Cold Cap

Thus, the consequence for the melting rate in different melters is clear in this case. Because the thickness of the gas layer will be very similar in both cases, the resistance for the heat flux through this secondary foam layer will be almost the same, resulting again in a comparable melting rate in both larger and smaller melters.

The phenomenon of the gas layer can also lead to an increase in the melting rate when considering bubbling. It is well known that big bubbles generated by the bubbler create vent holes. Through these vent holes, the gas from the gas layer under the cold cap can also escape, thus lowering the thickness of the gas layer, as illustrated in Figure 7.4:

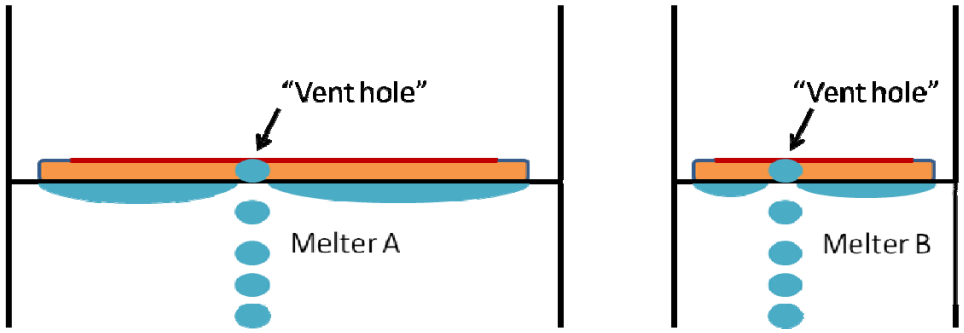

Figure 7.4. Vent Holes Created by Bubbling

The presence of the vent holes decreases the average width of the gas layer by creating more places where the gas can escape. This can in turn decrease the thickness of the gas layer. Thus, according to Fourier's law, the heat transfer to the cold cap will be higher, resulting in an increase in the melting rate.

8.0 Effect of Viscosity

In our model, the cold cap bottom boundary is set to where the flow can no longer be considered as vertical (one-dimensional), but it changes to the 3D flow of the molten glass.

Hence, this boundary can be identified with a certain critical value of viscosity. As the feed material proceeds through the cold cap and undergoes melting, it becomes less and less viscous. This is because the viscosity of the glass melt decreases dramatically with increasing temperature. The second important variable is then the melt composition. The melt viscosity increases as the fraction of dissolved silica increases.

In the extreme case, when no foam occurs, the transition from the 1D flow to the 3D flow will not be immediate, but rather gradual. In a real case, the melt at the bottom of the cold cap contains bubbles. According to Ishii (quoted by Pilon et al. [2006]),

$$\frac{\mu_C}{\mu_M} = \left(1 - \Phi\right)^{-1} \tag{8.1}$$

where μ_C is the viscosity of bubbly melt, μ_M is the viscosity of the bubble-free melt, and Φ is the void fraction. As this relationship indicates, the viscosity increases as the gas phase fraction increases because of the resistance of the bubbles to the deformation by the flow field.

Accordingly, a sharp viscosity increase can be expected in the secondary foam layer, resulting in a fast transition from the vertical 1D movement of the condensed phase to the 3D flow of molten glass and thus to a very thin thermal boundary layer.

Thus, one of the possible improvements of the model structure is the correlation of the bottom boundary to a certain value of viscosity. However, accurate experimental data are still not available.

9.0 Effect of Composition

In a report prepared by Vitreous State Laboratory (Matlack et al. 2010), the following conclusion was made: "Production rates are affected by the form of aluminum in the waste: a 35 to 40% rate increase was observed when changing from aluminum oxide to aluminum hydroxide, and a 25% rate increase was observed when changing from aluminum hydroxide to boehmite."

This conclusion establishes a plausible cause of the slow melting of the batch prepared with corundum (Al_2O_3) in conjunction with the large extent of foaming observed by Pierce et al. (submitted). Regarding the difference between the melting rate of feeds with aluminum hydroxide and boehmite, we may recollect that the melting rate is affected by the water content, both in the form of free water in slurry or bonded water in the form of hydroxides. This bonded water will increase the heat necessary to transport into the cold cap, thus slowing down the melting.

10.0 Conclusions and Future Work

The preliminary 1D model was successfully developed. The model equations were derived and processed by the finite difference method, allowing us to calculate the temperature field within the cold cap and to study the behavior of the cold cap under different boundary conditions. The results of feed melting crucible studies in addition to literature data were used as input data for the model.

Empirical data indicate that foaming has a strong impact on the melting rate. Therefore, further investigation in the area of the batch foaming will be necessary, both in terms of experiments and mathematical modeling. For a reliable prediction of the melting rate as a function of feed properties and melter conditions, future work will focus on the behavior of the foam layer at the bottom of the cold cap and the heat transfer through it.

To understand the formation and behavior of the foam layer, evolved gas analysis (EGA) will be also employed. Hopefully, it will provide us with a better insight into gas-evolving reactions in the high-temperature region (>700°C) where the thermo gravimetric measurements failed.

11.0 References

Choi AS, DH Miller, and DM Immel. 2010. "Determination of HLW Glass Melt Rate Using X-Ray Computed Tomography (CT)." SRNL-STI-2010-00767, Rev. 0, Savannah River National Laboratory, Aiken, South Carolina.

Henager SH, P Hrma, KJ Swearingen, MJ Schweiger, J Marcial, and NE TeGrotenhuis. 2011. "Conversion of batch to molten glass, I: Volume expansion." *J. Non-Cryst. Solids* 357:829–835.

Hrma P. 1982. "Thermodynamics of Batch Melting." *Glastechnische Berichte* 55:138.

Hrma P. 1990. "Melting of Foaming Batches: Nuclear Waste Glass." *Glastech. Ber.* 63K:360.

Hrma PR, MJ Schweiger, BM Arrigoni, CJ Humrickhouse, J Marcial, A Moody, C Rodriguez, RM Tate, and B Tincher. 2009. "Effect of Melter-Feed-Makeup on Vitrification Process." PNNL-18374, Pacific Northwest National Laboratory, Richland, Washington.

Hrma P, MJ Schweiger, CJ Humrickhouse, JA Moody, RM Tate, TT Rainsdon, NE TeGrotenhuis, BM Arrigoni, J Marcial, CP Rodriguez, and BH Tincher. 2010. "Effect of glass-batch makeup on the melting process." *Ceramics – Silikáty* 54(3):193–211.

Iguchi M, JO Ilegbusi. 2010. *Modeling Multiphase Materials Processes: Gas-Liquid Systems*. Springer, 1st edition, ISBN: 9781441974785.

Lottes SA and M Petrick. 2007. "Glass Furnace Model (GFM) Development and Technology Transfer Program." ANL-07/28, Argonne National Laboratory, Argonne, Illinois.

Matlack KS, H Gan, M Chaudhuri, W Kot, W Gong, T Bardakci, and IL Pegg, and J Innocent. 2010. "DM100 and DM1200 Melter Testing with High Waste Loading Glass Formulations for Hanford High-Aluminum HLW Streams." VSL-10R1690-1, Vitreous State Laboratory, The Catholic University of America, Washington, DC.

Perez JM, CC Chapman, RK Mohr, KS Matlack, and IL Pegg. 2005. "Development and demonstration of an air bubbler design to meet HLW melter production rate requirements of the Hanford waste treatment and immobilization plant." ICEM'05, 1260.

Pierce DA, P Hrma, J Marcial, BJ Riley, and MJ Schweiger. "Effect of alumina source on ease of melting of glass batch." *Int. Journal of Applied Glass Science*, submitted.

Pilon L, G Zhao, and R Viskanta. 2006. "Three-Dimensional Flow and Thermal Structures in Glass Melting Furnaces. Part II: Effect of Batch and Bubbles." *Glass Science and Technology* 75(3):115-124.

Raether F and M Krauss. 2004. "In situ measurements of batch glass during melting." *Glass Sci. Technol*. 77(3):118-123.

Schill P. 1982a. "Matematicky model taveni kmene v elektrickych pecich, Cast I: Teoreticke vztahy modelu." (In Czech), *Silikaty* 26:155.

Schill P. 1982b. "Matematicky model taveni kmene v elektrickych pecich, Cast II: Reseni modelovych rovnic." (In Czech) *Silikaty* 26:209.

Schill P. 2005. "Modeling the behavior of noble metals during HLW vitrification." In: W Lutze, *Modeling the behavior of noble metals during HLW vitrification in the DM1200 melter*. VSL-05R5740-1, Vitreous State Laboratory, Washington DC.

Viskanta R and X Wu. 1984. "Effect of Gas Percolation on Melting of Glass Batch." *Journal of the American Ceramic Society* 67(5):376-380.

Appendix A

Mathematical Model for the Determination of the True Effective Heat Conductivity

Appendix A: Mathematical Model for the Determination of the True Effective Heat Conductivity

Consider heating of a cylindrical crucible. In the simplest case, if we assume only heating from the sides, the heat equation can be written in 1D form as follows:

$$\rho c_p \frac{dT}{dt} = \lambda\left(\frac{\partial^2 T}{\partial r^2} + \frac{1}{r}\frac{\partial T}{\partial r}\right) + H(r,t) \tag{A.1}$$

where ρ, c_p, and λ are the density, heat capacity, and thermal conductivity of material inside the crucible, and $H(r,t)$ is the heat source (heat sink). As discussed, the DSC provides us with the values of c_p^{Eff}, which already "includes" the heat source term. Thus, the modified Equation 6.10 has form:

$$\rho c_p^{Eff} \frac{dT}{dt} = \lambda\left(\frac{\partial^2 T}{\partial r^2} + \frac{1}{r}\frac{\partial T}{\partial r}\right) \tag{A.2}$$

The solution of this Equation by the finite difference method, together with the defined boundary condition, will provide us with the temperature field inside the crucible. We can then determine the value of true effective heat conductivity by comparing the modeled and measured temperature field, assuming the density is known.

If the heat fluxes from the bottom or top cannot be neglected, the situation becomes 2D. A simple method was developed to solve this situation, based on the Finite Volume Method (FVM). Values of state variables (temperature) are calculated at discrete points on a meshed geometry, and the computational domain (crucible) is subdivided into finite volumes, as displayed in Figure A.1.

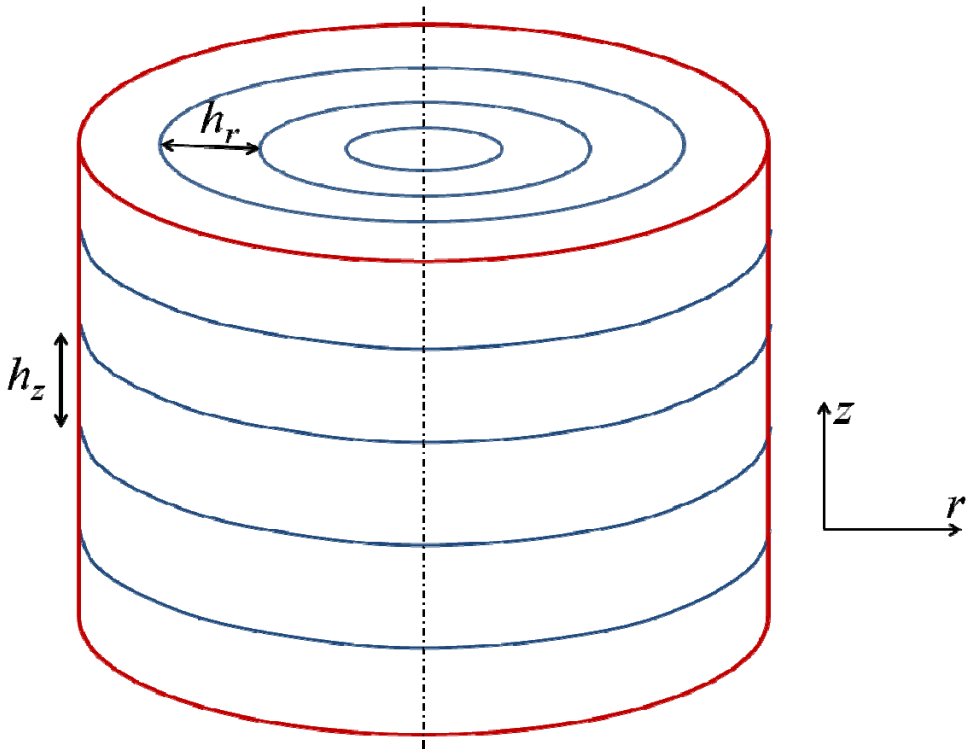

Figure A.1. The Computation Domain (crucible) Divided into Finite Volumes

Then, heat fluxes between each finite volume are expressed according to Fourier's law and used in the enthalpy balance of each finite volume:

$$\rho c_p^{Eff} \frac{dT_{k,l}}{dt} = A_{k-1} q_{k-1} - A_k q_k + A_{l-1} q_{l-1} - A_l q_l \qquad \text{(A.3)}$$

where A_k and A_{k-1} represent the area between adjacent finite volumes in a radial direction with respective heat fluxes q_k and q_{k-1}. Analogously, A_l and A_{l-1} represent the area between adjacent finite volumes in the axial direction with respective heat fluxes q_l and q_{l-1}. Together with defined boundary conditions, Equation A.3 will provide us with the time-dependent temperature field. This temperature field can be then used to calculate the temperature-dependent thermal conductivity, as was described before.

As an example, the simulated temperature field is shown in Figure A.2.

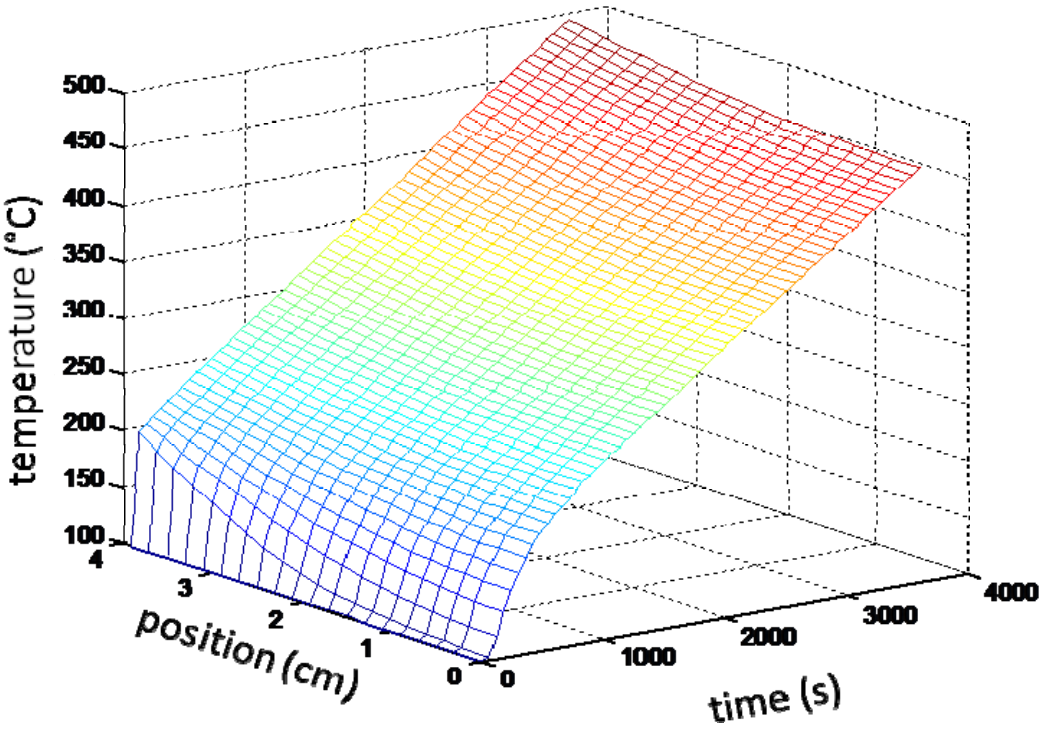

Figure A.2. Simulated Temperature Field Inside the Crucible

In this simulation, the crucible was preheated to 100°C at the beginning of the simulation (time = 0 s). Then, the temperature on the wall of the crucible (at 4 cm) was linearly increased (heating rate 5 K/min). Figure A.2 displays the change of temperature with time and position inside the crucible (the centre of crucible is positioned at 0). This model is ready to calculate the true value of heat conductivity as soon as temperature-distribution data are available.

Distribution*

U.S. Department of Energy
Office of Environmental Management
Kurt Gerdes
Steve Schneider
Gary Smith

U.S. Department of Energy
Office of River Protection
Tom Fletcher
Rob Gilbert
Albert Kruger
Billie Mauss
Stephen Pfaff

Energy Solutions
Innocent Joseph

Savannah River National Laboratory
Alexander Choi
Fabienne Johnson
David Peeler

Vitreous State Laboratory
Wing Kot
Ian Pegg

Waste Treatment and Immobilization Plant
Steve Barnes
Chris Chapman
Ernie Lee

Washington River Protection Solutions
Gene Ramsey
Terry Sams

Pacific Northwest National Laboratory
Paul Bredt
Jaehun Chun
Jarrod Crum
Pavel Hrma
Brad Johnson
Gary Josephson
Dong-Sang Kim
John McCloy
Reid Peterson
Loni Peurrung
Richard Pokorny
Brian Riley
Joseph Ryan
Mike Schweiger
Gary Sevigny
John Vienna
Joseph Westsik, Jr.

*Distribution will be made electronically.

Pacific Northwest
NATIONAL LABORATORY

U.S. DEPARTMENT OF
ENERGY

902 Battelle Boulevard
P.O. Box 999
Richland, WA 99352
1-888-375-PNNL (7665)
www.pnl.gov